nature climate change

Article

https://doi.org/10.1038/s41558-023-01915-x

Intensification of Pacific tropical instability waves over the recent three decades

Received: 18 May 2023

Accepted: 13 December 2023

Published online: 25 January 2024



Minyang Wang ¹, Shang-Ping Xie ², Hideharu Sasaki ³, Masami Nonaka ³ & Yan Du ^{1,4}

Tropical instability waves (TIWs) arise from shear instabilities of equatorial Pacific Ocean currents and are important for the tropical climate and the El Niño–Southern Oscillation. Yet the long-term evolution of TIW activity under climate change remains unclear due to the difficulty in estimating equatorial current velocity. Here we use in situ, satellite altimeter and sea surface temperature observations along with a realistic eddy-resolving ocean simulation to show that TIW activity has intensified in the central equatorial Pacific at $\sim\!12\pm6\%$ per decade over the recent three decades. The extended satellite data and the ocean model simulation show that the increased TIW activity is probably caused by an enhanced cross-equatorial asymmetric warming in the eastern tropical Pacific. The intensified TIWs lead to increased eddy dynamic heating effects of $\sim\!70\%$ since the 1990s near the equator, with implications for predicting and projecting tropical Pacific climate changes.

The equatorial Pacific cold tongue is a defining feature of the tropical climate system affecting the global climate¹ (Fig. 1a). Generated by shear instabilities of equatorial zonal currents, tropical instability waves (TIWs)²⁻⁵ create meanders of the cold tongue visible in satellite images of sea surface temperature (SST)^{6,7} (Fig. 1b). TIWs are characterized by quasi-monthly oscillations of meridional flows propagating westward from the eastern to the central equatorial Pacific with wavelengths of 1,000-2,000 km (refs. 8,9). TIWs play profound roles in equatorial multiscale ocean dynamics. They extract energy from ocean mean flows^{10,11}, interacting with the atmosphere^{12,13} through SST, radiating waves (energy) to deep14,15 and subtropical16 oceans, inducing buoyant gravity currents¹⁷ and internal solitary waves¹⁸, and dissipating energy to turbulence 19,20. In addition, TIWs play essential roles in modulating the mean state and variability of the tropical climate²¹ and marine ecosystem²² through eddy advection²³, rectified effects on mean flows^{24,25} and mixing²⁶⁻²⁸. For example, they influence El Niño-Southern Oscillation (ENSO), including variance^{29,30}, asymmetry^{21,31}, irregularity³² and future change³³, by modifying the cold tongue heat balance. Understanding the evolution of TIWs is crucial to predicting and projecting tropical Pacific climate changes.

TIW activity is high during boreal summer to winter with prevailing trade winds that force strong zonal currents, triggering shear instabilities^{34,35}. On the interannual timescale, TIWs are anomalously strong in La Niña years while weak in El Niño events³⁶. Through eddy dynamic heating effects³⁷, they contribute to ENSO asymmetry by preferentially damping La Niña²⁹⁻³¹. Because of limited observations of near-equatorial ocean currents, the long-term change of TIW activity, for example, in the face of a warming climate or internal climate variability, remains unclear. Over the past three decades, the tropical Pacific has undergone a La Niña-like mean state change³⁸, with a strengthened Walker circulation³⁹ and intensified cross-equatorial winds⁴⁰. TIWs might be sensitive to equatorial ocean circulation changes in response to the mean state change. A recent study 41 reported a decrease in mesoscale variability in tropical oceans over the satellite altimetry era (1993-2020). However, the change in TIWs was not explored because the geostrophic calculation fails near the equator 42.

Geostrophic calculation with altimeter-observed sea surface height (SSH) is widely used to estimate surface currents off the equator by geostrophic balance between the Coriolis force and the pressure gradient force. At the equator, the Coriolis force goes to zero and the

¹State Key Laboratory of Tropical Oceanography, South China Sea Institute of Oceanology, Chinese Academy of Sciences, Guangzhou, China. ²Scripps Institution of Oceanography, University of California San Diego, La Jolla, CA, USA. ³Application Laboratory, Japan Agency for Marine-Earth Science and Technology, Yokohama, Japan. ⁴University of Chinese Academy of Sciences, Beijing, China. Ee-mail: sxie@ucsd.edu; duyan@scsio.ac.cn

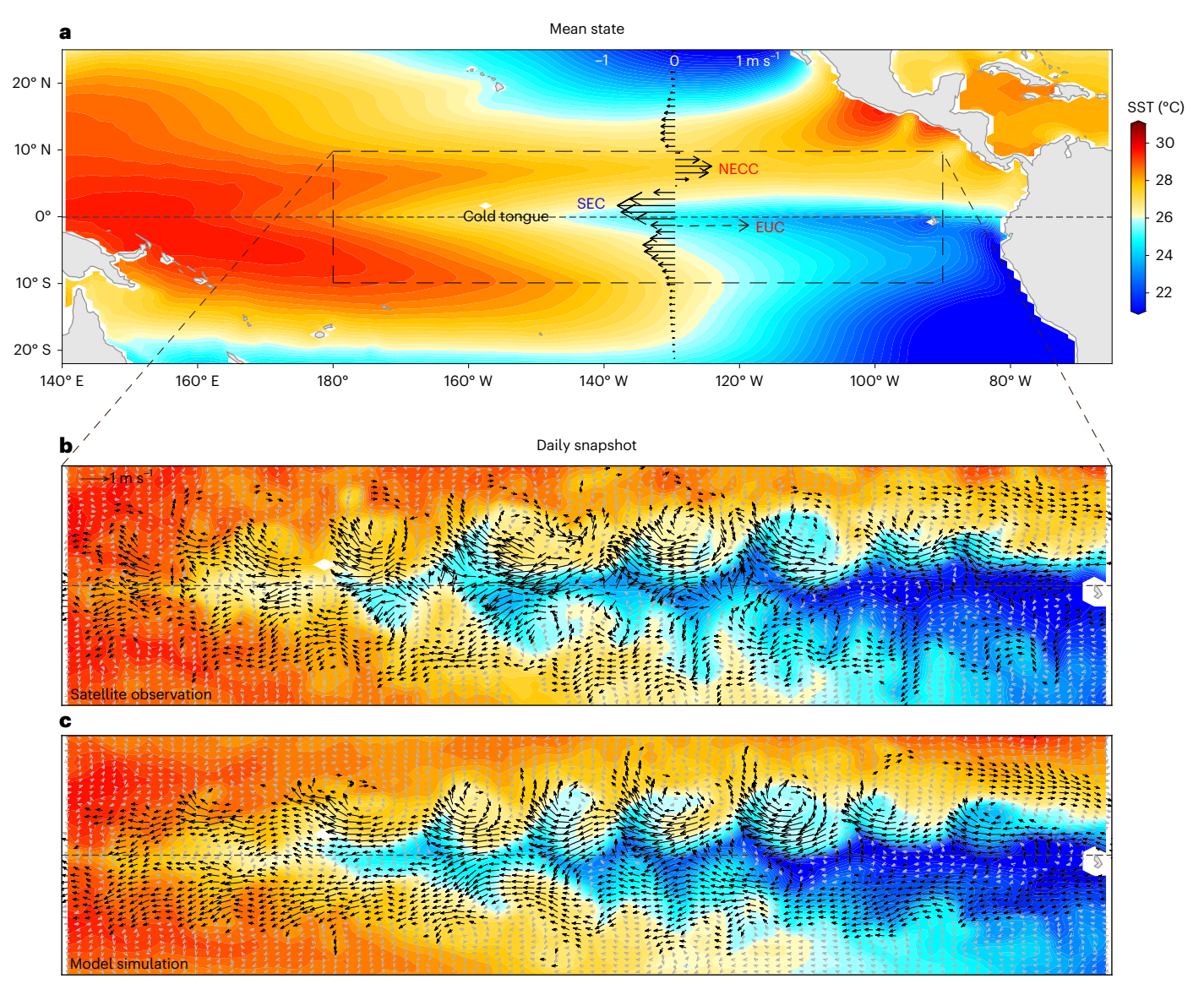


Fig. 1 | Sea surface temperature and velocity in the tropical Pacific. a, Satellite-observed June–February mean SST and a profile of zonal currents at 130° W; NECC, SEC and EUC denote the surface North Equatorial Countercurrent, South Equatorial Current and subsurface Equatorial Undercurrent (~100 m depth),

respectively. **b**, Snapshot of satellite-observed SST (colour coding same as in **a**) and altimeter-derived surface velocity (vector, >0.3 m s⁻¹ in black) on 15 August 2016. **c**, Same as **b** but for model simulation (OFES2). The meanders of cold tongue in **b** and **c** signify TIWs.

geostrophic calculation does not apply to estimate eddy flows of TIWs. TIWs consist of Rossby and Yanai modes, characterized by oscillations of meridional flows trapped around 4° N and the equator with periods of $\sim\!\!33$ d and $13\!-\!27$ d, respectively 4,8,43 . Flows of the Rossby mode are quasi-geostrophic, while those of the Yanai mode are ageostrophic near the equator. The motions of the Yanai mode are controlled by the balance between inertial forces (local accelerations and nonlinear advection) and the pressure gradient force. By considering the inertial forces, we have recently developed a shallow water diagnostic model to compute both the Rossby and Yanai modes of TIW flows from altimeter-observed SSH 4 (Fig. 1b vectors), which can be used to investigate the long-term change in TIWs since 1993.

In this study, we examine the multidecadal evolution of TIW activity using four independent datasets: satellite observations of SSH (1993–2021) and SST (1982–2021), in situ measurements of current velocity (1980s–2020) from equatorial moorings and a global eddy-resolving hindcast (1958–2021) from the Ocean General Circulation Model for the Earth Simulator v.2 (OFES2 (refs. 44–46); Fig. 1c) that is forced with reanalysis atmospheric forcing⁴⁷. We also use a

global ocean eddy-resolving reanalysis (GLORYS12V1) 48 to compare our results and the high-resolution model intercomparison project v1.0 endorsed by the coupled model intercomparison project phase 6 (CMIP6 HighResMIP1) ensemble 49 to discuss TIW responses to external radiative forcing. We compute the trends using linear regression and a modified Mann–Kendall test 41,50 (Methods). Our results reveal intensified TIWs in the central equatorial Pacific over 1993–2021.

Trends over 1993-2021

TIWs induce strong meanders of the equatorial cold tongue, quantified by the variance of high-pass filtered meridional SST gradient (SST $_y^2$) (Extended Data Fig. 1a and Methods). The satellite-observed mean $\overline{\text{SST}'_y}^2$ peaks at the equator (Fig. 2a contours) due to the combined effects of the cold tongue trough intensity ($\overline{\text{SST}}_{yy}^2$) and the variance of meridional flows of Yanai-mode TIWs ($\overline{v'^2}$) (equation (3) in Methods). Over the satellite altimetry period (1993–2021), the $\overline{\text{SST}'_y}^2$ has statistically significantly increased by 28 ± 9% per decade near the equator

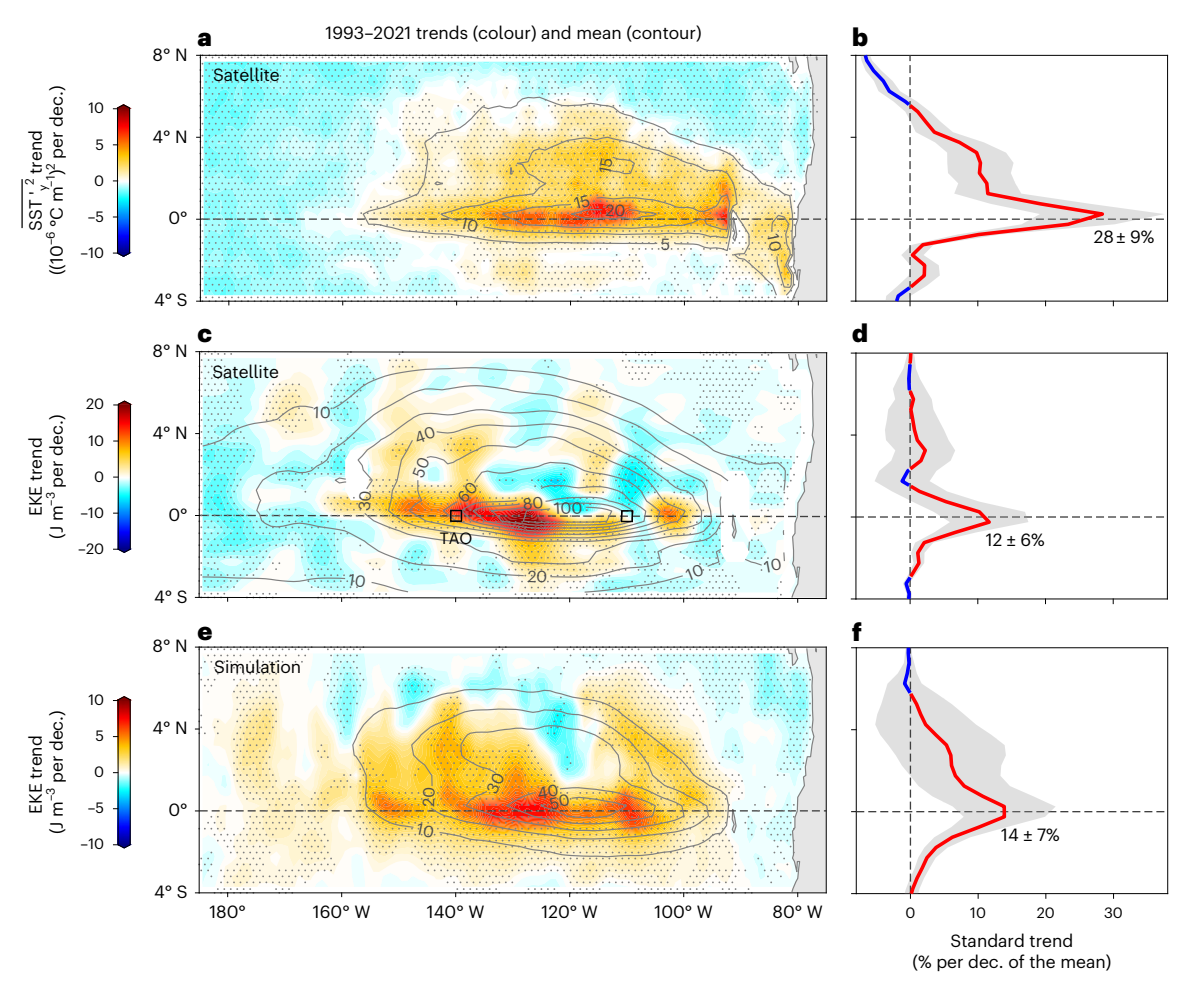


Fig. 2 | **Trends of TIW intensity.** 1993–2021 trends (colour shading) are superimposed on the mean states (contour, same unit as the trends without 'per dec.'). **a**, Satellite-observed $\overline{\text{SST}'_y}^2$. **c**, Satellite altimeter-derived EKE. **e**, OFES2-simulated surface EKE. **b**,**d**,**f**, 160° W–100° W average of **a**,**c**,**e**, along with the uncertainties (grey shading) in percentage, standardized using the maximum values of the climatological mean in the meridional direction. Data are

presented as trends \pm uncertainties (estimated as the s.e.m.; Methods) at the equator, with n=27,26 and 25 for $\bf b$, $\bf d$ and $\bf f$, respectively. The two squares in $\bf c$ denote equatorial moorings at 140° W and 110° W equator of the TAO array. Throughout the paper, the trends were calculated on the basis of the 9-yr running mean time series at each location (Methods; annual mean-based results are shown in Extended Data Fig. 2). Dotted regions pass the 95% confidence level based on the modified Mann–Kendall test (hereafter the same).

(Fig. 2b; see Methods and Extended Data Fig. 2 for definitions of the trend, significance and uncertainty). The cold tongue trough intensity (\overline{SST}_{yy}^2) strengthened at $16 \pm 9\%$ per decade (Extended Data Fig. 3a). The difference between the trends in \overline{SST}_y^2 and \overline{SST}_{yy}^2 suggests an intensification of $\overline{v'^2}$ of ~12% per decade near the equator.

Surface eddy kinetic energy (EKE) represents the dynamic intensity of TIWs. Using a diagnostic model, we derive TIW surface flows and EKE from multi-altimeter-merged SSH observations (see Methods and Extended Data Fig. 4 for model equations and validations). The derived EKE captures the Yanai mode peaking on the equator (\geq 80 J m $^{-3}$) and the Rossby mode north of the equator (\geq 40 J m $^{-3}$) (Fig. 2c contours). The EKE trend reveals intensified TIW activity in the central equatorial Pacific (Fig. 2c colour shading). The increasing rate reaches $12\pm6\%$ (\sim 8 \pm 4 J m $^{-3}$) per decade of the mean at the equator (Fig. 2d), comparable to high-latitude EKE trends 41 . Specifically, the altimeter-derived kinetic energy spectrum clarifies that the trend is dominated by the Yanai mode (wide-band ranging from 13–27 d) rather than the Rossby mode (\sim 33 d) (Extended Data Fig. 1c). Combined with the strengthened $\overline{\rm SST}_{yy}^{\ 2}$, the intensified $\overline{v'}^{\ 2}$ of the Yanai mode indeed explains the $\overline{\rm SST}_{y}^{\ 2}$ trend (Extended Data Fig. 3a–d). The in situ observations of mooring

at 140° W equator shows a surface-amplified increase in EKE of \sim 10 J m⁻³ (\sim 16% of the mean) per decade over 1993–2020 at 30 m depth (Extended Data Fig. 4b), validating the satellite results.

Meridional velocity of Yanai-mode TIWs is associated with cross-equatorial pressure gradient force⁴, corresponding to the elevated $\overline{\text{SSH}'_y}^2$ near the equator observed by satellite altimeters (Extended Data Fig. 5b red curve). The observed $\overline{\text{SSH}'_y}^2$ has significantly increased near the equator as ground truth for the derived EKE trend (Extended Data Fig. 5a red curve). The 1/12° GLORYS12V1 reanalysis assimilates satellite observations, including along-track altimeter data^{28,48}. Both the $\overline{\text{SSH}'_y}^2$ and EKE of GlORYS12V1 show intensified TIW activity (Extended Data Fig. 5 magenta curves) while underestimating Yanai and overestimating Rossby mode trends compared with observations, possibly due to biases in data assimilation. The reanalysis also

demonstrates the relationship between the trends of $\overline{v'^2}$ and $\overline{SST'_y}^2$ at the equator (Extended Data Fig. 3e-h).

We use an eddy-resolving hindcast simulation with OFES2 to investigate the dynamics of observed trends. The OFES2 simulates meanders of the cold tongue (Fig. 1c) and the meridional structures of EKE of the Yanai and Rossby modes (Fig. 2e contours) (see Methods for detailed

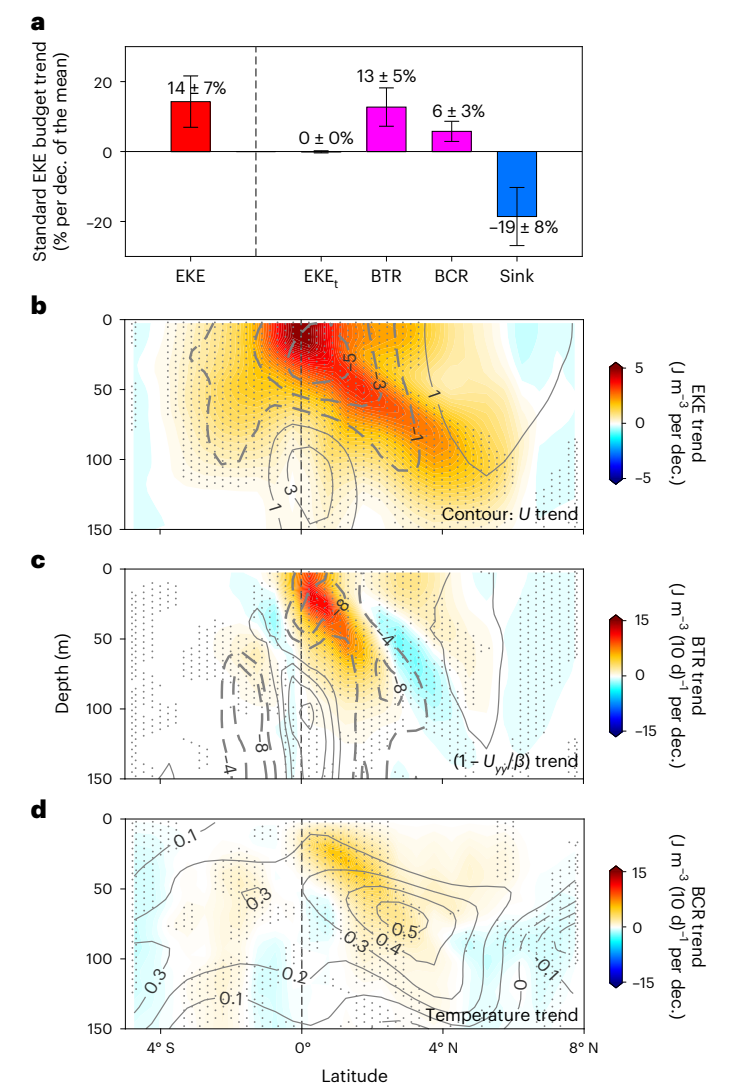


Fig. 3 | **Trends of EKE budget based on OFES2 simulation. a**, 1993–2021 trends of EKE (standardized using the mean EKE) and EKE budget terms (standardized using the sum of mean BTR and BCR), including EKE tendency, BTR, BCR and energy sink (shaded bars, averaged between 160° W -100° W, 2° S -2° N and 0-50 m depth). Error bars denote uncertainties as the s.e.m. Data are presented as trends \pm uncertainties, with n=24, 28, 26, 24 and 25 from left to right. **b**–**d**, Meridional transects of trends of EKE (colour shading) with zonal current (contour, cm s $^{-1}$ per decade) (**b**), BTR (colour shading) with $(1-U_{yy}/\beta)$ (contours, 10^{-2} per decade) (**c**) and BCR (colour shading) with temperature (contour, $^{\circ}$ C per decade) (**d**), 160° W -100° W averaged.

validations). The simulated EKE captures intensified Yanai-mode TIWs, increasing at $14\pm7\%$ per decade (Fig. 2f), in broad agreement with observations and physically consistent with the strengthened mean flows (Extended Data Fig. 5e). The simulated SST $_y^2$ trend is biased to be negative due to weakened curvature of the mean SST profile at the equator (Extended Data Fig. 3i–l). Compared with the observed warming that is larger north than south of the equator, the OFES2 simulates a larger warming near the equator (Extended Data Fig. 5g), possibly due to biases in the atmospheric forcing and/or oceanic vertical mixing. The model, however, successfully simulates the increased variance of cross-equatorial meridional flows (Extended Data Fig. 3j).

Although each has its own weaknesses, the four independent datasets: satellite SST, SSH and in situ current observations as well as an eddy-resolving model simulation, taken together, corroborate that Yanai-mode TIW activity has intensified in the

central equatorial Pacific at ${\sim}12\pm6\%$ per decade for EKE over the recent three decades.

EKE budget

To identify energy sources of the intensified TIWs, we conduct a simplified EKE budget analysis on the basis of the OFES2 output (Methods). To leading order, TIWs derive kinetic energy from the meridional shear and available potential energy of the background zonal currents¹¹ while losing energy to friction and the radiation of waves^{14–16}. The simulation indicates that in the mean state, the barotropic conversion from mean flows dominates (\sim 65% of) the total energy source, while the baroclinic conversion contributes ~35%, both with large interannual variability (Extended Data Fig. 6a). The results are consistent with previous satellite-based evaluations^{4,34} as OFES2 captures the basic structures of equatorial currents and stratification (Extended Data Fig. 6b,d). The trends in the energy conversion rates indicate that the increased barotropic instabilities (13 \pm 5% per decade of the mean total energy source) predominate the energy source of the intensified TIWs, while the increased baroclinic instabilities ($6 \pm 3\%$ per decade) play a secondary role (Fig. 3a).

Anecessary condition for barotropic instability is that the gradient of the absolute vorticity of the background circulation, $\beta - U_{yy}$, changes sign²⁵. With strong shears of the Equatorial Undercurrent (EUC) and North Equatorial Countercurrent (NECC), the south and north flanks of the South Equatorial Current (SEC) generally satisfy the condition (Extended Data Fig. 6b,c contours). The multidecadal variability of TIW EKE is indeed highly correlated with the SEC speed (Extended Data Fig. 6e black curve). Over the recent three decades, the OFES2 simulates an accelerating SEC asymmetrically north of the equator (Fig. 3b contours), corroborated by the satellite-derived and reanalysis results (Extended Data Fig. 5e). As the SEC acceleration strengthens the current shears and barotropic instabilities near the equator (Fig. 3c), the Yanai-mode TIWs intensify by gaining more energy from the mean flows.

In addition, changes in upper ocean stratifications and meridional buoyancy fronts could impact TIW intensity through baroclinic instabilities^{33,51}. The Institute of Atmospheric Physics, Chinese Academy of Sciences (IAP, CAS) temperature and salinity reconstructions⁵² based on in situ observations show decreased upper ocean stratification in the mixed layer due to the subsurface-amplified warming (Extended Data Fig. 7a,c). The OFES2 captures the subsurface-amplified warming and decreased ocean stratification above (Extended Data Fig. 7b,d). Specifically, the subsurface-amplified warming strengthens the buoyancy fronts near the equator (Extended Data Fig. 7e,f). The decreased stratification and strengthened buoyancy fronts indicate more available potential energy that could feed the TIW activity, as a secondary mechanism for the intensified TIWs (Fig. 3d).

Increased TIW EKE indicates more energy cascades or radiations to turbulence or deep oceans. The decreased upper ocean stratification and intensified Yanai-mode TIWs could promote turbulent mixing in the upper edge of the EUC by modulating the vertical shear ^{19,20}. The stronger background buoyancy fronts and TIW-induced buoyancy front variance could generate more buoyant gravity currents ¹⁷ and internal solitary waves ¹⁸ that cascade energy to small scales. Furthermore, the intensified Yanai-mode TIWs could radiate a stronger downward-propagating beam of Yanai waves that may enhance the Equatorial Intermediate Current system ¹⁴. Further studies are needed to explore the effects of intensified TIWs on the multiscale ocean dynamic changes.

Drivers of TIW trends

In situ and satellite observations along with a realistic ocean model simulation consistently show intensified Yanai-mode TIWs over the recent three decades. A question arises: is the 30-yr trend part of multidecadal variability or representing a monotonic change, for example,

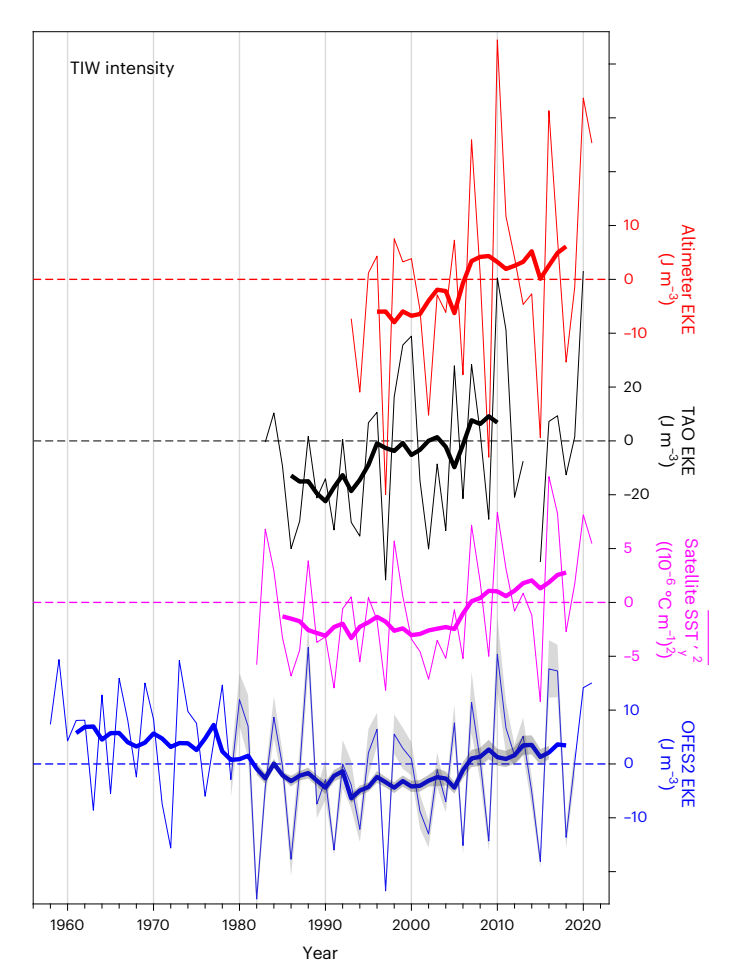


Fig. 4 | **Multidecadal variability of TIW intensity.** Annual mean (thin curves) and decadal mean (bold curves; 9-yr running average) time series of satellite altimeter-derived EKE (red), in situ EKE (black) from TAO (140° W, 0°) at 30 m depth, satellite $\overline{SST'}_y^2$ (magenta) and OFES2-simulated surface EKE (blue), averaged between 160° W–100° W and 1° S–1° N, 1993–2021 mean removed. The grey shading on the blue curves denotes the spread (1 s.d.) among 10 members of the OFES2 ensemble for 1979–2019.

due to global warming? To investigate this question, we analyse the full-length time series of TIW intensity, especially from the extended satellite SST data and OFES2 simulation (Fig. 4). A 9-yr running average removes the dominant interannual variability (thin curves) and isolates the long-term evolution of TIW intensity (bold curves). The results from the four datasets are mutually consistent. The altimeter-derived EKE increases for 1993–2021 (bold red curve), a trend that the moored observations confirm before 2010 (bold black curve). The time series

of satellite SST $_y^2$ hint at a likely multidecadal variability of TIWs—decreasing from 1982 to the 1990s and then increasing to the present (bold magenta curve). The OFES2 simulation (thin blue curve) is correlated at 0.79, 0.88 and 0.95 with moored current measurements, satellite SST and altimetry observations for the annual mean time series, respectively. The high cross-correlations among independent datasets and with the ocean model simulations give confidence in our estimates of TIW intensity variability. Over the 64-yr period, the OFES2-simulated TIW activity had weakened from the 1960s to the 1990s and has since recovered (bold blue curve) with small spreads among OFES2 ensemble members 46 (grey shading), partially corroborated by the satellite SST data available since the 1980s. The satellite SST and OFES2 simulation suggest that the recent trend from the 1990s is probably part of a multidecadal variability.

To understand the underlying drivers of the recent trend or multidecadal variability of TIWs, we investigate the trends and multidecadal variability of tropical Pacific climate and ocean circulation using satellite observations, OFES2 and reanalyses (Fig. 5). The OFES2 simulation well captures the climate mean state⁴⁴, large-scale structure of the trends (Extended Data Fig. 8) and the multidecadal variability (Fig. 5b,d). In the mean state, the eastern tropical Pacific exhibits a cross-equatorial meridional asymmetry with the Intertropical Convergence Zone (ITCZ) staying north of the equator⁵³ (Fig. 1a). The associated cross-equatorial southeasterly trade winds drive the strongly sheared zonal currents for the TIW generation and seasonality^{34,54}.

Over the recent three decades, the satellite-observed SST data show a marked increase in the climatic asymmetry (Fig. 5a). The cross-equatorial SST difference indicates that the asymmetry increases from the 1990s (Fig. 5b). Coupled with the enhanced asymmetry, the southeasterly winds strengthen across the equator (Fig. 5a red vectors). The winds drive the sea level to rise faster at 5° N than to the south (Fig. 5c). The increased meridional sea level gradient yields an accelerating SEC at ~0.07 m s⁻¹ per decade near 140° W (Fig. 5c red vectors), resulting in intensified TIWs. The longer time series of SEC from OFES2 and ORAS5 reanalysis further reveal that the SEC speed has undergone a V-shaped multidecadal variability since the 1960s with the inflection in the 1990s (Fig. 5d). Consequently, the TIW activity exhibits a similar V-shaped variability, as captured by the OFES2 simulation and corroborated partially by the satellite SST data (Fig. 4). Taken together, these results suggest that TIW activity has intensified since the 1990s as part of the V-shaped multidecadal variability, driven by the cross-equatorial asymmetric warming in the eastern tropical Pacific.

Discussion

Our study has revealed a robust multidecadal change in Pacific TIWs. TIWs have intensified at $\sim\!12\pm6\%$ per decade over the recent three decades as part of a V-shaped variability since the 1960s, a finding corroborated mutually by in situ, satellite observations, a global eddy-resolving ocean simulation (OFES2) and reanalyses. Our results show that the recent trend since the 1990s is probably due to a rapid intensification of cross-equatorial asymmetry of the eastern Pacific climate, with the enhanced southerly winds and SEC acceleration.

The intensified TIW activity in recent decades contrasts with recent results from eddy-resolving global climate models with increased greenhouse gas (GHG) forcing 33,51, which project an El Niño-like warming state and decreased TIW activity in the tropical Pacific. The results might be model-dependent. Nevertheless, this suggests that the intensified TIWs and strengthened climatic asymmetry since the 1990s are possibly due to internal variability 55,56 (for example, the Interdecadal Pacific Oscillation) and/or other anthropogenic effects 57,58 (for example, aerosol radiative forcing), rather than a simple response to increased GHG forcing. On the other hand, the intensified TIW activity is distinct from high-latitude eddy activity 41,59, which has shifted poleward, associated with the poleward expansion of ocean gyres and enhanced subpolar fronts 60,61.

To explore the response of TIW activity to external radiative forcing, we evaluate the long-term evolution of $\overline{SST'}_y^2$ in the historical vs SSP585 (very high GHG emissions) scenario runs of the CMIP6 High-ResMIP1 (ref.49). The multimodel ensemble captures the climatological mean structure of $\overline{SST'}_y^2$, characterized by a peak at the equator (Extended Data Fig. 9a). The historical ensemble shows an increased $\overline{SST'}_y^2$ at $7\pm8\%$ per decade over 1993–2014 (Extended Data Fig. 9b bold blue curve), only a quarter of the observed trend. In contrast, the SSP585 ensemble projects a decreased $\overline{SST'}_y^2$ at $-4\pm5\%$ per decade over 2015–2050 (bold red curve). Only half of the six models simulate statistically significant trends (Extended Data Fig. 9d,e markers with

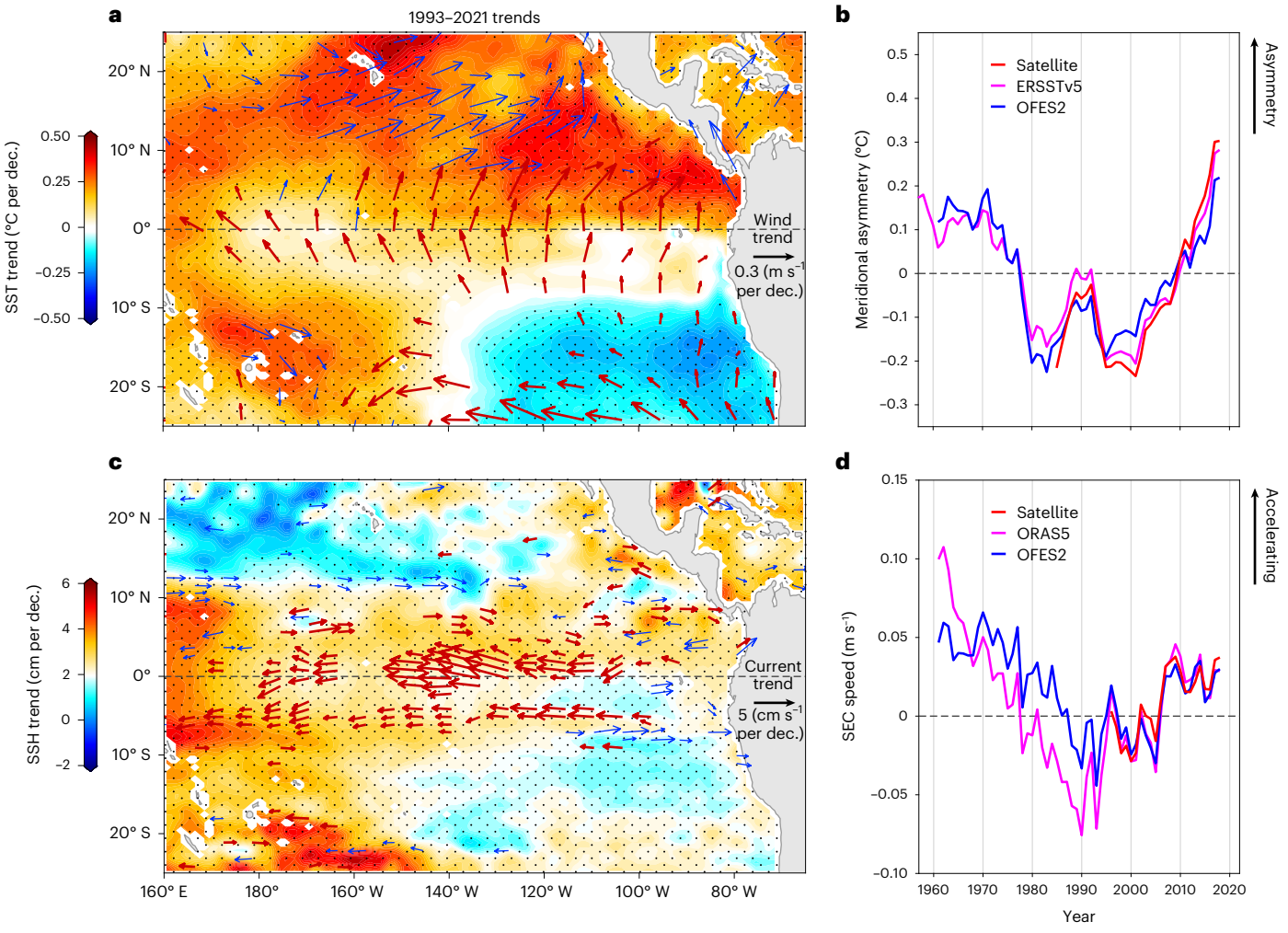


Fig. 5 | Trends of the tropical Pacific climate and ocean circulation. a, 1993–2021 trends of satellite-observed SST (colour shading) and 10 m wind (vector, accelerating in bold red; decelerating in thin blue). b, Time series of cross-equatorial SST difference between 0° – 15° N and 15° S -0° , 160° W -80° W box mean, from satellite (red), ERSSTv5 (magenta) and OFES2 (blue).

c,1993-2021 trends of satellite altimeter-observed SSH (colour shading) and OSCAR2 currents (vector, accelerating in bold red; decelerating in thin blue). d, Time series of SEC speed averaged between $0^\circ-4^\circ$ N, 160° W– 100° W, from OSCAR2 (red), ORAS5 (magenta) and OFES2 (blue). Time series were smoothed by a 9-yr running average, 1993-2021 mean removed.

black edges), with large inter-model spreads. The large uncertainty of the TIW response to external forcing is possibly due to model independence and the small ensemble number. The weak-biased trend in the historical ensemble mean suggests that the observed trend is possibly dominated by internal variability rather than external forcing. With the caveat of only six models and large uncertainties, the contrast between the historical run vs SSP585 suggests that TIWs may respond to different radiative forcing in distinct ways, a tantalizing possibility that needs to be critically investigated.

TIWs have two-way interactive effects on the cold tongue heat balance: a direct effect through eddy dynamic heating 23,29 (EDH; Methods) and a rectified effect through upscaling feedback on mean flows 10,24,25 . Most state-of-the-art climate models do not resolve or under-represent TIW dynamics because of insufficient horizontal resolution ($\geq 1^{\circ}$) 62 , causing biases in the simulated mean state and variability of the equatorial Pacific climate. Eddy-resolving climate models 33,51 significantly reduce the cold tongue bias 1 (anomalously cooler cold tongue than observation) compared with the CMIP6 ensemble, suggesting the importance of TIWs for the Pacific mean state. A recent study 25 shows that an ocean model of 1° resolution simulates $\sim 50\%$ weaker TIW activity and $\sim 1^{\circ}$ C cooler cold tongue compared with the same model of $1/12^{\circ}$ resolution. The 1° -resolution model reproduces

the rectified effect of reducing the mean flow (EUC) strength but fails to simulate the EDH warming effect. Coarse-resolution models may underestimate the narrow (\sim 1° S-1° N) Yanai mode more than the broad (\sim 2° N-6° N) Rossby mode, leading to a large underestimation of EDH near the equator⁶³.

On the basis of satellite SST and altimeter-derived TIW surface flows, we identify that the TIW-induced EDH is of the same order of magnitude as the ENSO-associated nonlinear dynamic heating (~2 °C month⁻¹)⁶⁴ at the surface (Extended Data Fig. 10a). Such a heating effect has significantly increased at \sim 23 ± 9% per decade (\sim 70% over the recent three decades; Extended Data Fig. 10b), which favours the observed moderate warming of SST at the equator (Fig. 5a). The downward trend in TIW activity projected in future climate CMIP6 (with large uncertainties) raises many important questions about the contribution of the two-way upscaling effects from TIWs vs GHG forcing to the eastern tropical Pacific mean state change. For example, the decreased TIW activity could reduce the warming effect of EDH, which may enhance La Niña, reduce ENSO asymmetry and weaken the El Niño-like mean state change projected by most climate models⁶⁵. Therefore, the long-term evolution of TIWs and their effects must be carefully considered when evaluating projected mean state changes under future climate.

Online content

Any methods, additional references, Nature Portfolio reporting summaries, source data, extended data, supplementary information, acknowledgements, peer review information; details of author contributions and competing interests; and statements of data and code availability are available at https://doi.org/10.1038/s41558-023-01915-x.

References

- Li, G. & Xie, S.-P. Tropical biases in CMIP5 multimodel ensemble: the excessive equatorial Pacific cold tongue and double ITCZ problems. J. Clim. 27, 1765–1780 (2014).
- Willett, C. S., Leben, R. R. & Lavín, M. F. Eddies and tropical instability waves in the eastern tropical Pacific: a review. *Prog. Oceanogr.* 69, 218–238 (2006).
- Holmes, R. M., Thomas, L. N., Thompson, L. & Darr, D. Potential vorticity dynamics of tropical instability vortices. *J. Phys.* Oceanogr. 44, 995–1011 (2014).
- Wang, M., Xie, S.-P., Shen, S. S. P. & Du, Y. Rossby and Yanai modes of tropical instability waves in the equatorial Pacific Ocean and a diagnostic model for surface currents. *J. Phys. Oceanogr.* 50, 3009–3024 (2020).
- Kennan, S. C. & Flament, P. J. Observations of a tropical instability vortex. J. Phys. Oceanogr. 30, 2277–2301 (2000).
- Shi, W. & Wang, M. Tropical instability wave modulation of chlorophyll-a in the Equatorial Pacific. Sci. Rep. 11, 22517 (2021).
- 7. Zheng, G., Li, X., Zhang, R. H. & Liu, B. Purely satellite data-driven deep learning forecast of complicated tropical instability waves. *Sci. Adv.* **6**, eaba1482 (2020).
- Lyman, J. M., Johnson, G. C. & Kessler, W. S. Distinct 17- and 33-day tropical instability waves in subsurface observations. *J. Phys. Oceanogr.* 37, 855–872 (2007).
- Liu, C., Wang, X., Köhl, A., Wang, F. & Liu, Z. The northeastsouthwest oscillating equatorial mode of the tropical instability wave and its impact on equatorial mixing. *Geophys. Res. Lett.* 46, 218–225 (2019).
- Brown, J. N., Godfrey, J. S. & Wijffels, S. E. Nonlinear effects of tropical instability waves on the equatorial Pacific circulation. J. Phys. Oceanogr. 40, 381–393 (2010).
- Holmes, R. M. & Thomas, L. N. Modulation of tropical instability wave intensity by equatorial Kelvin waves. J. Phys. Oceanogr. 46, 2623–2643 (2016).
- Small, R. J. et al. Air-sea interaction over ocean fronts and eddies. Dyn. Atmos. Oceans 45, 274–319 (2008).
- Li, T., Yu, Y., An, B., Luan, Y. & Chen, K. Tropical instability waves in a high-resolution oceanic and coupled GCM. *Ocean Model.* 182, 102169 (2023).
- Ascani, F., Firing, E., Dutrieux, P., McCreary, J. P. & Ishida, A. Deep equatorial ocean circulation induced by a forced-dissipated Yanai beam. J. Phys. Oceanogr. 40, 1118–1142 (2010).
- Tanaka, Y., Hibiya, T. & Sasaki, H. Downward lee wave radiation from tropical instability waves in the central equatorial Pacific Ocean: a possible energy pathway to turbulent mixing.
 J. Geophys. Res. Oceans 120, 7137–7149 (2015).
- Farrar, J. T. Barotropic Rossby waves radiating from tropical instability waves in the Pacific Ocean. J. Phys. Oceanogr. 41, 1160–1181 (2011).
- Warner, S. J. et al. Buoyant gravity currents released from tropical instability waves. J. Phys. Oceanogr. 48, 361–382 (2018).
- Santos-Ferreira, A. M., da Silva, J. C. B., St-Denis, B., Bourgault, D. & Maas, L. R. M. Internal solitary waves within the cold tongue of the Equatorial Pacific generated by buoyant gravity currents.
 J. Phys. Oceanogr. https://doi.org/10.1175/JPO-D-22-0165.1 (2023).
- Holmes, R. M. & Thomas, L. N. The modulation of equatorial turbulence by tropical instability waves in a regional ocean model. J. Phys. Oceanogr. 45, 1155–1173 (2015).

- Inoue, R., Lien, R.-C., Moum, J. N., Perez, R. C. & Gregg, M. C. Variations of equatorial shear, stratification, and turbulence within a tropical instability wave cycle. *J. Geophys. Res. Oceans* 124, 1858–1875 (2019).
- 21. Imada, Y. & Kimoto, M. Parameterization of tropical instability waves and examination of their impact on ENSO characteristics. *J. Clim.* **25**, 4568–4581 (2012).
- 22. Eddebbar, Y. A. et al. Seasonal modulation of dissolved oxygen in the equatorial Pacific by tropical instability vortices. *J. Geophys. Res. Oceans* **126**, e2021JC017567 (2021).
- 23. Jochum, M. & Murtugudde, R. Temperature advection by tropical instability waves. *J. Phys. Oceanogr.* **36**, 592–605 (2006).
- Maillard, L., Boucharel, J. & Renault, L. Direct and rectified effects of tropical instability waves on the eastern tropical Pacific mean state in a regional ocean model. J. Phys. Oceanogr. 52, 1817–1834 (2022).
- Maillard, L., Boucharel, J., Stuecker, M. F., Jin, F.-F. & Renault, L. Modulation of the Eastern Equatorial Pacific seasonal cycle by tropical instability waves. *Geophys. Res. Lett.* 49, e2022GL100991 (2022).
- Moum, J. N. et al. Sea surface cooling at the equator by subsurface mixing in tropical instability waves. *Nat. Geosci.* 2, 761–765 (2009).
- Cherian, D. A. et al. Off-equatorial deep-cycle turbulence forced by tropical instability waves in the equatorial Pacific. *J. Phys.* Oceanogr. 51, 1575–1593 (2021).
- 28. Whitt, D. B. et al. Simulation and scaling of the turbulent vertical heat transport and deep-cycle turbulence across the equatorial Pacific cold tongue. *J. Phys. Oceanogr.* **52**, 981–1014 (2022).
- 29. Xue, A., Zhang, W., Boucharel, J. & Jin, F. F. Anomalous tropical instability wave activity hindered the development of the 2016/17 La Niña. *J. Clim.* **34**, 5583–5600 (2021).
- 30. Wang, S. et al. El Niño/Southern Oscillation inhibited by submesoscale ocean eddies. *Nat. Geosci.* **15**, 112–117 (2022).
- An, S.-I. Interannual variations of the tropical ocean instability wave and ENSO. J. Clim. 21, 3680–3686 (2008).
- 32. Holmes, R. M., McGregor, S., Santoso, A. & England, M. H. Contribution of tropical instability waves to ENSO irregularity. *Clim. Dyn.* **52**, 1837–1855 (2019).
- 33. Wengel, C. et al. Future high-resolution El Niño/Southern Oscillation dynamics. *Nat. Clim. Change* **11**, 758–765 (2021).
- 34. Wang, M., Du, Y., Qiu, B., Xie, S.-P. & Feng, M. Dynamics on seasonal variability of EKE associated with TIWs in the eastern equatorial Pacific Ocean. *J. Phys. Oceanogr.* **49**, 1503–1519 (2019).
- 35. Wang, M. et al. Mechanism of seasonal eddy kinetic energy variability in the eastern equatorial Pacific Ocean. *J. Geophys. Res.* Oceans **122**, 3240–3252 (2017).
- 36. Boucharel, J. & Jin, F.-F. A simple theory for the modulation of tropical instability waves by ENSO and the annual cycle. *Tellus A* **72**, 1–14 (2020).
- Xue, A., Jin, F.-F., Zhang, W., Boucharel, J. & Kug, J.-S.
 Parameterizing the nonlinear feedback on ENSO from tropical instability waves (TIWs) by nonlinear eddy thermal diffusivity.
 Clim. Dyn. https://doi.org/10.1007/s00382-023-06744-4 (2023).
- 38. Kosaka, Y. & Xie, S.-P. Recent global-warming hiatus tied to equatorial Pacific surface cooling. *Nature* **501**, 403–407 (2013).
- 39. England, M. H. et al. Recent intensification of wind-driven circulation in the Pacific and the ongoing warming hiatus. *Nat. Clim. Change* **4**, 222–227 (2014).
- 40. Hu, S. N. & Fedorov, A. V. Cross-equatorial winds control El Niño diversity and change. *Nat. Clim. Change* **8**, 798–802 (2018).
- Martínez-Moreno, J. et al. Global changes in oceanic mesoscale currents over the satellite altimetry record. *Nat. Clim. Change* 11, 397–403 (2021).

- Johnson, E. S., Bonjean, F., Lagerloef, G. S., Gunn, J. T. & Mitchum, G. T. Validation and error analysis of OSCAR sea surface currents. J. Atmos. Ocean. Technol. 24, 688–701 (2007).
- 43. He, W.-B., Yang, Y. & San Liang, X. Mechanisms for generating and connecting the Yanai-mode and Rossby-mode tropical instability waves in the equatorial Pacific. *Deep Sea Res. I Oceanogr. Res. Pap.* **197**, 104041 (2023).
- 44. Sasaki, H. et al. A global eddying hindcast ocean simulation with OFES2. Geosci. Model Dev. 13, 3319–3336 (2020).
- Sasaki, H., Qiu, B., Klein, P., Nonaka, M. & Sasai, Y. Interannual variations of submesoscale circulations in the subtropical northeastern Pacific. *Geophys. Res. Lett.* 49, e2021GL097664 (2022).
- Nonaka, M., Sasaki, H., Taguchi, B. & Schneider, N. Atmospheric-driven and intrinsic interannual-to-decadal variability in the Kuroshio Extension jet and eddy activities. *Front. Mar. Sci.* 7, 547442 (2020).
- 47. Tsujino, H. et al. JRA-55 based surface dataset for driving ocean–sea-ice models (JRA55-do). Ocean Model. **130**, 79–139 (2018).
- 48. Jean-Michel, L. et al. The Copernicus global 1/12 oceanic and sea ice GLORYS12 reanalysis. *Front. Earth Sci.* **9**, 698876 (2021).
- Haarsma, R. J. et al. High resolution model intercomparison project (HighResMIP v1.0) for CMIP6. Geosci. Model Dev. 9, 4185–4208 (2016).
- Yue, S. & Wang, C. The Mann–Kendall test modified by effective sample size to detect trend in serially correlated hydrological series. Water Resour. Manage. 18, 201–218 (2004).
- Wang, S. et al. Weakened submesoscale eddies in the equatorial Pacific under greenhouse warming. *Geophys. Res. Lett.* 49, e2022GL100533 (2022).
- Li, G. et al. Increasing ocean stratification over the past half-century. Nat. Clim. Change 10, 1116–1123 (2020).
- 53. Xie, S.-P. et al. Eastern Pacific ITCZ dipole and ENSO diversity. *J. Clim.* **31**, 4449–4462 (2018).
- 54. Imada, Y., Kimoto, M. & Chen, X. Impact of the atmospheric mean state on tropical instability wave activity. *J. Clim.* **25**, 2341–2355 (2012).
- Friedman, A. R., Hwang, Y. T., Chiang, J. C. & Frierson, D. M. Interhemispheric temperature asymmetry over the twentieth century and in future projections. J. Clim. 26, 5419–5433 (2013).

- Meehl, G. A., Hu, A., Arblaster, J. M., Fasullo, J. & Trenberth, K.
 E. Externally forced and internally generated decadal climate variability associated with the Interdecadal Pacific Oscillation. *J. Clim.* 26, 7298–7310 (2013).
- 57. Watanabe, M. & Tatebe, H. Reconciling roles of sulphate aerosol forcing and internal variability in Atlantic multidecadal climate changes. *Clim. Dyn.* **53**, 4651–4665 (2019).
- Kang, S. M., Xie, S.-P., Deser, C. & Xiang, B. Zonal mean and shift modes of historical climate response to evolving aerosol distribution. Sci. Bull. 66, 2405–2411 (2021).
- 59. Beech, N. et al. Long-term evolution of ocean eddy activity in a warming world. *Nat. Clim. Change* **12**, 910–917 (2022).
- Yang, H. et al. Poleward shift of the major ocean gyres detected in a warming climate. *Geophys. Res. Lett.* 47, e2019GL085868 (2020).
- 61. Shi, J.-R., Talley, L. D., Xie, S.-P., Peng, Q. & Liu, W. Ocean warming and accelerating Southern Ocean zonal flow. *Nat. Clim. Change* **11**, 1090–1097 (2021).
- Chassignet, E. P. et al. Impact of horizontal resolution on global ocean–sea ice model simulations based on the experimental protocols of the Ocean Model Intercomparison Project phase 2 (OMIP-2). Geosci. Model Dev. 13, 4595–4637 (2020).
- 63. Graham, T. The importance of eddy permitting model resolution for simulation of the heat budget of tropical instability waves. Ocean Model. **79**, 21–32 (2014).
- 64. An, S.-I. & Jin, F.-F. Nonlinearity and asymmetry of ENSO. *J. Clim.* **17**, 2399–2412 (2004).
- 65. Shin, N.-Y. et al. More frequent central Pacific El Niño and stronger eastern Pacific El Niño in a warmer climate. *NPJ Clim. Atmos. Sci.* **5**, 101 (2022).

Publisher's note Springer Nature remains neutral with regard to jurisdictional claims in published maps and institutional affiliations.

Springer Nature or its licensor (e.g. a society or other partner) holds exclusive rights to this article under a publishing agreement with the author(s) or other rightsholder(s); author self-archiving of the accepted manuscript version of this article is solely governed by the terms of such publishing agreement and applicable law.

© The Author(s), under exclusive licence to Springer Nature Limited 2024

Methods

Datasets

For satellite observations, we used daily Optimum Interpolation SST from the National Oceanic and Atmospheric Administration (NOAA OISST v.2.1), daily SSH from the Archiving, Validation and Interpretation of Satellite Oceanographic data (AVISO) of the Copernicus Marine Environment Monitoring Service (CMEMS), monthly Ocean Surface Current Analysis Real-time (OSCAR v.2.0) from the NASA Physical Oceanography Distributed Active Archive Center (PO, DAAC) and monthly 10-m wind velocity from NOAA National Centers for Environmental Information (NCEI) Blended Seawinds (NBS v.2.0).

For in situ observations, we used daily velocity merged from current metre and acoustic Doppler current profiler (ADCP) measurements of two moorings of the Tropical Atmosphere Ocean (TAO) array at the equator 140° W and 110° W from the NOAA Pacific Marine Environmental Laboratory (PMEL), drifter-derived climatological monthly mean zonal currents from the Physical Oceanography Division (PhOD) NOAA 66, and reconstructed monthly ocean temperature and salinity from IAP, CAS⁵².

For ocean model simulations, we used the quasi-global, eddy-resolving OFES2 developed at the Japan Agency for Marine-Earth Science and Technology (JAMSTEC). The horizontal grid spacing is ~10 km on the equator. OFES2 includes a sea-ice model and a tidal mixing scheme, and is forced by a surface atmospheric dataset called JRA55-do (JRA55-based surface dataset for driving ocean-sea-ice model). The OFES2 hindcast is available from 1958 to the near present⁴⁴. In addition, a 10-member ensemble integration of OFES2 was made from 1965 to 2019 (OFES2 ensemble hereafter) to isolate the oceanic intrinsic variability unrelated to atmospheric forcing. Member runs differ only in initial conditions, obtained by sampling the original OFES2 hindcast every 2 d over an 18-d period between 3 and 21 January 1965 (see ref. 46 for details). We used the daily output of the OFES2 ensemble available between 1979-2019. The small ensemble spread of TIW EKE (Fig. 4 grey shading) gives confidence in the robust response of TIWs to the atmospheric forcing.

For coupled atmosphere–ocean model simulations, we used the daily SST output of CMIP6 HighResMIP1 ensemble 49 , including 6 models, to explore the role of multidecadal variability vs monotonic changes in TIW activity (Extended Data Fig. 9). The models are EC-Earth3P-HR (2 members), HaDGEM3-GC31-HH, CNRM-CM6-1-HR (3 members), CMCC-CM2-VHR4, CMCC-CM2-HR4 and FGOALS-f3-H. Their atmosphere model part has a resolution of $\sim\!1^{\circ}$, while the resolution of the ocean part is $\leq\!0.25^{\circ}$. We chose the models that provide both the historical and the future SSP585 runs.

For reanalysis datasets, we used the daily SSH and surface current velocity from the CMEMS global ocean eddy-resolving (1/12° horizontal resolution, 50 vertical levels) reanalysis (GLORYS12V1)⁴⁸ covering the altimetry (1993 onward) to cross-validate the altimeter-derived EKE trend (Extended Data Fig. 5). For analyses of tropical Pacific mean state changes (Fig. 5), we used monthly SST from the NOAA Extended Reconstructed SST (ERSST v.5), monthly current from the European Centre for Medium-Range Weather Forecasts (ECMWF) estimation of ocean state via Ocean ReAnalysis System 5 (ORAS5) and monthly 10-m wind velocity from the JRA55-do reanalysis of the Japan Meteorological Agency (Extended Data Fig. 8a vectors).

TIW variability and two-dimensional (2D) high-pass filtering

We first averaged the daily datasets into a 3-d interval on a 0.5°-latitude \times 1°-longitude grid before analyses. According to the zonal wavenumber-frequency spectra (Extended Data Fig. 1 contours), we defined and isolated TIW variability by high-pass filtering with a cut-off period of 40 d and a cut-off westward wavelength of 3,000 km via 2D discrete fast Fourier transforms (2DFFT). For in situ velocity from TAO, we isolated TIW variability by 40-d high-pass filtering. As the trends of SST, SSH, SST $_y$ or kinetic energy spectra are robust in the TIW

spectral domain (Extended Data Fig. 1 colour shading), our results are insensitive to slight changes in spatio-temporal filtering.

TIW-induced variance of cross-equatorial SST gradient

As meridional flows (v') of TIWs induce SST fluctuations (SST') on background SST fronts (\overline{SST}_y) , we have an approximate relationship between them (note that this is a proportional formula rather than an equation, as the left and right terms have no equal unit and are not in phase):

$$SST' \propto -\nu' \overline{SST}_{\nu} \tag{1}$$

where the prime and overbar denote the high-pass TIW variability and the monthly mean, respectively. The equivalent variability in meridional SST gradient is

$$SST'_{y} \propto -v'\overline{SST}_{yy} - v'_{y}\overline{SST}_{y}. \tag{2}$$

At the cold tongue trough (near the equator), $\overline{SST}_{\nu} = 0$ and

$$\overline{\text{SST'}_{y}^{2}} \propto \overline{v'^{2}} \left(\overline{\text{SST}}_{yy}\right)^{2}. \tag{3}$$

The variance of the cross-equatorial SST gradient $\overline{SST'_y}^2$ is a good indicator for the TIW current variance $\overline{v'}^2$ at the equator, which is hard to measure, as the cold tongue trough $\left(\overline{SST}_{yy}\right)^2$ is confined at the equator. Extended Data Fig. 2 demonstrates the relationship in equation (3) for the long-term trend with three different datasets.

Annual mean and mean state

Considering the TIW seasonality, we defined the annual mean of TIW intensity and also large-scale processes at year 0 as the average from June (0) to February (+1) throughout the study. The mean state is defined as the average of the annual mean over 1993–2021.

Trends, significance and uncertainties

The interannual variability associated with ENSO (with a period of 2–8 yr) is dominant in the annual mean time series of TIW intensity (Extended Data Fig. 2a,c,e thin curves), which would cause large uncertainty of the trend calculation over the 29-yr-long record (1993–2021). For example, whether the ending year of the record is El Niño or La Niña impacts the trend calculation of TIW intensity (thin dashed lines). To identify a trend independent of ENSO phases, we used a 9-yr running mean (with the first and last 4 yr dropped) rather than the annual mean time series to calculate the trends and statistical significance (bold dashed line).

On the basis of the 9-yr running mean time series, we calculated the trends and statistical significance using a linear least-squares regression and a modified Mann-Kendall test^{41,50}, respectively. The statistical test considers effective sample size (n number), taking into account autocorrelations within time series. Note that the 9-yr running mean increases the statistical significance from 90-95% to 99% confidence level (Extended Data Fig. 2a,c,e Pvalues). The annual mean time series-based statistical significance shows that some positive trends at and south of the equator pass the 95% confidence level even in the presence of interannual variability (Extended Data Fig. 2b,d,f). Finally, we report the uncertainties of the trend calculations (mostly due to interannual variability) as the s.e.m.⁴¹ (error bars in Figs. 2b,d,f and 3a, and Extended Data Fig. 3): s.e.m. = $\frac{\text{s.d.}}{\sqrt{n}}$, where n is the number of detrended annual mean time series. The percentage form of the trend and uncertainty was standardized using the maximum value of the climatological mean in the space. The uncertainties of the mean states were measured using the s.d. (error bars in Fig. 4, and Extended Data Figs. 4b, e, 6a and 9).

Shallow water diagnostic model and EKE

We estimated TIW surface velocity (u', v') from the filtered SSH (h') of AVISO with a diagnostic model⁴ as follows:

$$\left(\frac{\partial}{\partial t} + \delta^{x}\right)u' + Uu'_{x} - \left(f - U_{y}\right)v' = -gh'_{x},\tag{4}$$

$$\left(\frac{\partial}{\partial t} + \delta^{y}\right)v' + Uv'_{x} + fu' = -gh'_{y},\tag{5}$$

where the letters with prime denote the 40-d and 3,000-km 2D high-pass filtered fields. U denotes the basic state of surface ocean circulation, obtained using the monthly zonal current of OSCAR2. The subscripts (x and y) refer to the zonal and meridional partial differentiation, respectively; f is the Coriolis parameter; g is the gravity acceleration; and the Rayleigh damping rates $\delta^x = (7d)^{-1}$ and $\delta^y = (4d)^{-1}$ for the zonal and meridional momentum equations, respectively. The MATLAB code and the input data for the model are available in the repository 67 (https://doi.org/10.6084/m9.figshare.24633606.v1). The results of (u', v') were validated with TAO moorings in our previous study 4 .

Then, the TIW-associated EKE was defined as:

$$EKE = \frac{1}{2}\rho_0 \left(\overline{u'^2} + \overline{v'^2} \right), \tag{6}$$

where the constant ocean water density $\rho_0=$ 1, 024 kg m⁻³, the overbar denotes monthly average and EKE has a unit of J m⁻³.

Validations of altimeter-derived and OFES2 EKE with TAO moorings

The magnitudes of altimeter-derived EKE were close to mooring observations near the surface, including the multidecadal change and interannual variability (Extended Data Fig. 4). The variance correlation coefficients (*r*) reached 0.84 and 0.37 at 140° W and 110° W equator, significant above the 95% and 90% confidence levels, respectively.

The OFES2-simulated EKE was biased lower by $\sim 50\%$ than the observations possibly due to the underestimated SEC and NECC (Extended Data Fig. 5f blue curve). Despite this, the model captured the interannual variability of the EKE (Extended Data Fig. 4c,f blue curves) as forced with reanalysis atmospheric forcing ⁴⁷. The r with TAO moorings reached 0.73 and 0.46 at 140° W and 110° W equator, both significant above the 95% confidence level.

TIW EKE budget

To identify energy sources for the TIW trend, we analysed a simplified budget (the complete form refers to previous studies^{11,43}) of the TIW-associated EKE on the basis of the OFES2 output:

$$EKE_{t} = BTR + BCR + Sink (residual), (7)$$

where the barotropic conversion rate (BTR) and baroclinic conversion rate (BCR) are two well-known energy sources for TIW generation. They are given by:

$$BTR \approx -\rho_0 U_{\nu} \overline{u'v'}, \tag{8}$$

$$BCR = -g\overline{\rho' w'},\tag{9}$$

where the overbar and capital letter denote the monthly average, ρ' and w' are the TIW-scale filtered density and vertical velocity anomalies, respectively, and ρ_0 is the constant density. In equation (8), we only retained the dominant term and neglected $-\rho_0 U_x \overline{u'u'}$, $-\rho_0 V_x \overline{u'v'}$ and $-\rho_0 V_y \overline{v'v'}$, which are small or negative 24,35. Positive BTR (BCR) indicates barotropic (baroclinic) instability, transferring energy from the mean kinetic energy (eddy potential energy) to EKE. The energy sink by friction or energy radiation was estimated as the residual.

As TIWs have an e-folding time of \sim 2 weeks, we show BTR or BCR in a unit of J m⁻³ (10 d)⁻¹. Due to the short e-folding time, the interannual³⁴,

multidecadal variability or long-term trend of EKE is in phase with and proportional to the energy sources (Extended Data Fig. 6e) but not the accumulation of energy sources, as the energy is quickly generated and dissipated. For the budget analysis (Extended Data Fig. 6a or Fig. 3a), each term in equation (7) was standardized using the total energy source (sum of climatological mean BTR and BCR).

TIW-induced FDH

We calculated the surface and subsurface TIW-induced EDH on the basis of the satellite observations/deviations and OFES2 output, respectively, as:

$$EDH_{surface} = -\overline{u'SST'_{x}} - \overline{v'SST'_{y}}, \tag{10}$$

$$EDH_{subsurface} = -\overline{u'\theta'_x} - \overline{v'\theta'_y} - \overline{w'\theta'_z}, \tag{11}$$

where (u',v',w') are the 3D components of TIW velocity and θ' is the TIW-induced ocean water temperature fluctuation. They act to modulate the heat balance in the cold tongue region by nonlinear eddy advections of ocean heat, shown with a unit of °C month⁻¹. Positive (negative) EDH represents local warming (cooling) effects.

Data availability

The NOAA OISST v.2.1 is available at https://www.ncei.noaa.gov/data/ sea-surface-temperature-optimum-interpolation/v2.1/. The AVISO SSH is available at https://resources.marine.copernicus.eu/product-detail/ SEALEVEL GLO PHY L4 NRT OBSERVATIONS 008 046/DATA-ACCESS. The OSCAR v.2.0 is available at https://doi.org/10.5067/OSCAR-25F20. The NOAA NBS v.2.0 wind is available at https://www.ncei.noaa.gov/ products/blended-sea-winds. The TAO observations are available at https://www.pmel.noaa.gov/tao/drupal/disdel/. The drifter-derived climatological mean zonal currents are available at https://www. aoml.noaa.gov/phod/gdp/mean_velocity.php. The reconstruction dataset for temperature and salinity is available at http://www.ocean. iap.ac.cn/?navAnchor=home. The OFES2 simulation and 10-member ensemble output are available at https://www.jamstec.go.jp/ofes/ofes2. html. The GLORYS12V1 is available at https://data.marine.copernicus. eu/product/GLOBAL MULTIYEAR PHY 001 030/description. The ERSST v.5 is available at http://apdrc.soest.hawaii.edu/dods/public data/NOAA SST/ERSST/monthly v5. The ECMWF ORAS5 reanalysis is available at https://cds.climate.copernicus.eu/cdsapp#!/dataset/ reanalysis-oras5?tab=form. The JMA JRA55-do reanalysis is available at https://climate.mri-jma.go.jp/pub/ocean/JRA55-do/. The CMIP6 High-ResMIP1 ensemble is available at https://esgf-node.llnl.gov/projects/ cmip6/. The processed data⁶⁸ used in this study are publicly available in MATLAB format at https://doi.org/10.6084/m9.figshare.24633639.

Code availability

The diagnostic model ⁶⁷ for the TIW surface currents is available at https://doi.org/10.6084/m9.figshare.24633606.v1 via MATLAB codes. All analyses and figures ⁶⁸ in this manuscript are reproducible via MATLAB codes found in the repository (https://doi.org/10.6084/m9.figshare.24633639).

References

- Laurindo, L. C., Mariano, A. J. & Lumpkin, R. An improved near-surface velocity climatology for the global ocean from drifter observations. *Deep Sea Res. I Oceanogr. Res. Pap.* 124, 73–92 (2017).
- 67. Wang, M. A diagnostic model for TIW currents from SSH. Dataset. *figshare* https://doi.org/10.6084/m9.figshare.24633606.v1 (2023).
- Wang, M. Intensification of Pacific tropical instability waves over the recent three decades. Dataset. figshare https://doi. org/10.6084/m9.figshare.24633639.v1 (2023).

Acknowledgements

M.W. and Y.D. at SCSIO/CAS were supported by the National Natural Science Foundation of China (42090042, 42106024) and the Chinese Academy of Sciences (133244KYSB20190031, 183311KYSB20200015, LTOZZ2203, SCSIO202201). S.-P.X. was supported by the US NSF (AGS 2105654). H.S. was supported by JSPS KAKENHI Grant Number JP19H05701. The numerical computation was supported by the Earth Simulator in the Japan Agency for Marine-Earth Science and Technology (JAMSTEC), and the High-Performance Computing Division in the South China Sea Institute of Oceanology, Guangzhou, China.

Author contributions

M.W., S.-P.X. and Y.D. conceived the study. M.W. conducted the analyses, wrote the initial manuscript draft and produced all figures. H.S. conducted the global ocean model simulation (OFES2), and M.N. conducted the OFES2 ensemble simulations. All authors contributed to the interpretation of the results and the writing and revision of the paper.

Competing interests

The authors declare no competing interests.

Additional information

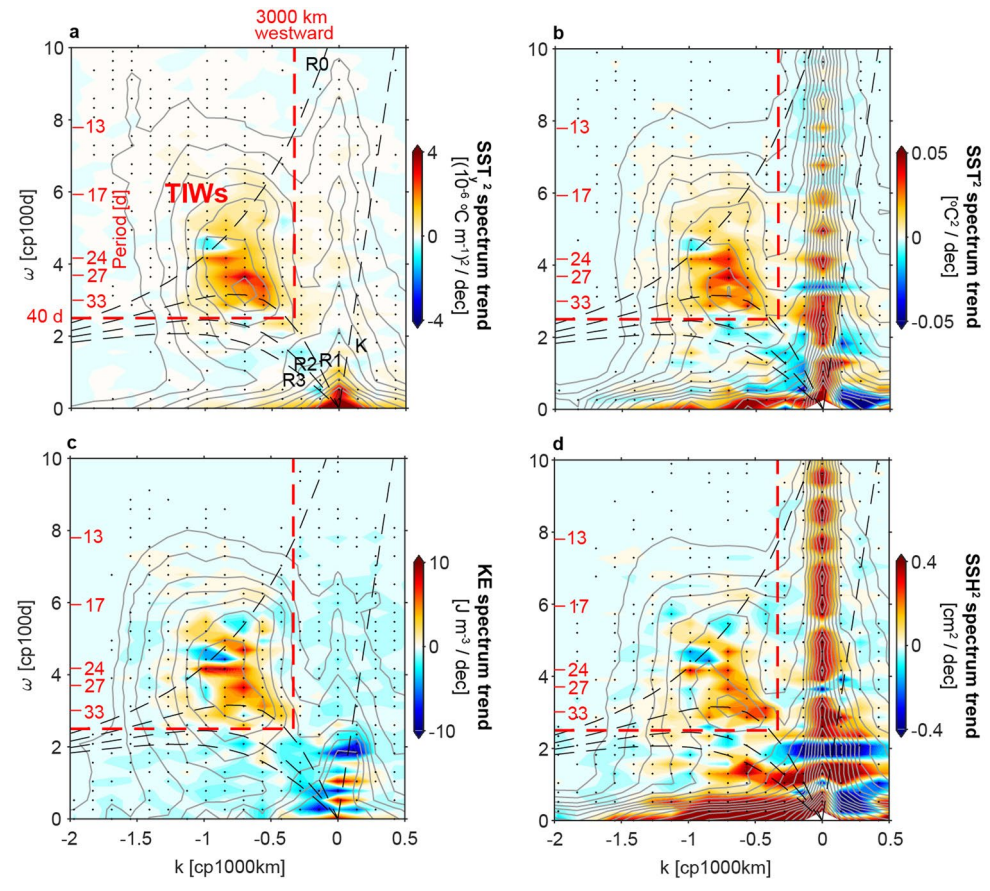
Extended data is available for this paper at https://doi.org/10.1038/s41558-023-01915-x.

Supplementary information The online version contains supplementary material available at https://doi.org/10.1038/s41558-023-01915-x.

Correspondence and requests for materials should be addressed to Shang-Ping Xie or Yan Du.

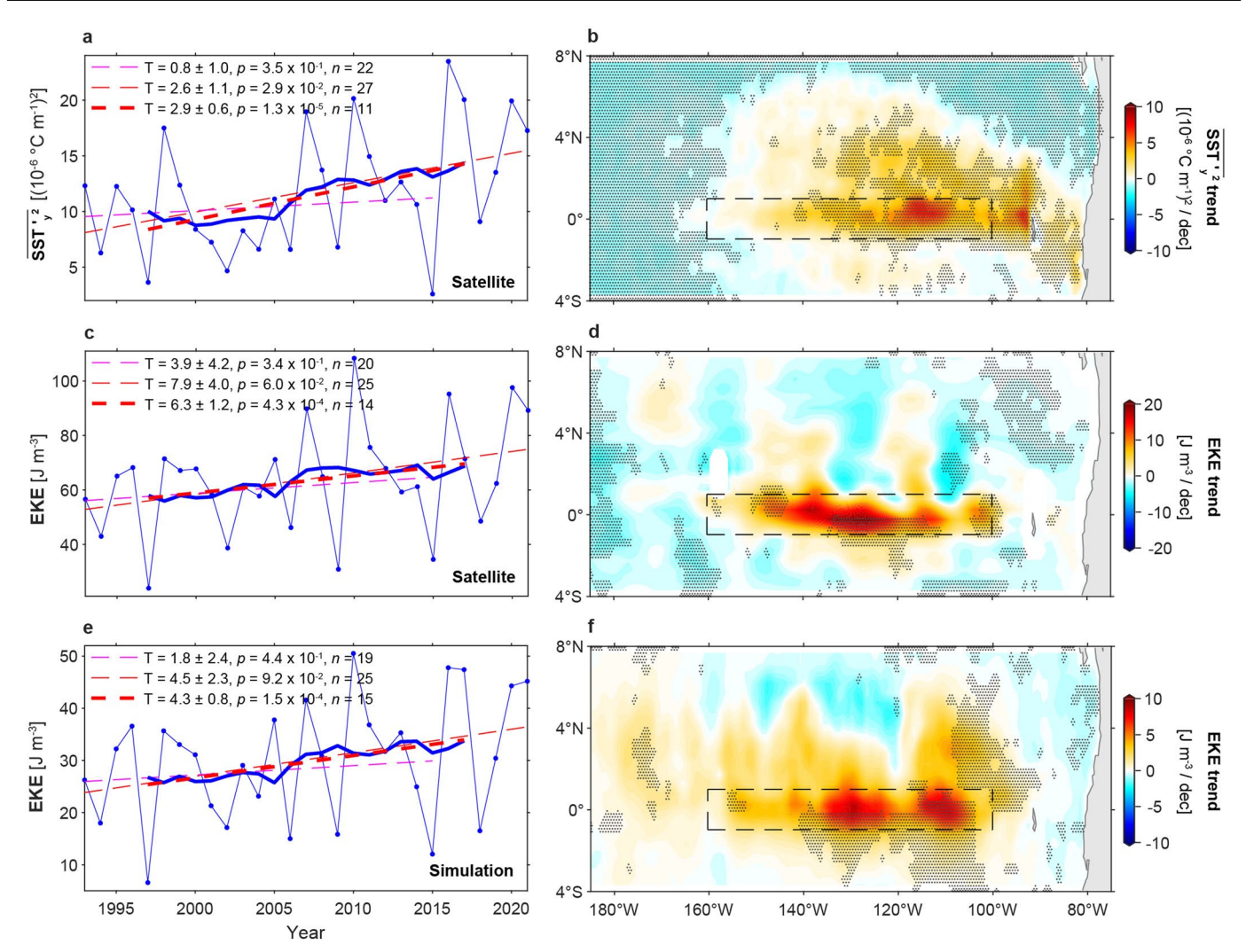
Peer review information *Nature Climate Change* thanks Julien Boucharel, Ryan Holmes and the other, anonymous, reviewer(s) for their contribution to the peer review of this work.

 $\label{lem:compression} \textbf{Reprints and permissions information} \ is \ available \ at \\ www.nature.com/reprints.$



Extended Data Fig. 1| **Observed trends of equatorial wavenumber-frequency spectra.** 1993–2021 trends (color shading) are superimposed with the mean states (contour, in log scale): **a**, SST, variance spectrum, contour initiating from -0.8 with interval of 0.2, $(10^{-6}\,^{\rm oC}\,{\rm m}^{-1})^2$; **b**, SST variance spectrum, contour initiating from -2.6 with interval of 0.2, $^{\rm oC}$; **c**, SSH-derived surface kinetic energy (KE) spectrum, contour initiating from -0.2 with interval of 0.2, J m $^{-3}$; **d**, SSH variance spectrum, contour initiating from -1.4 with interval of 0.2, cm 2 . The period is shown on the y-axis in red text. Red dashed box represents the TIW spectral

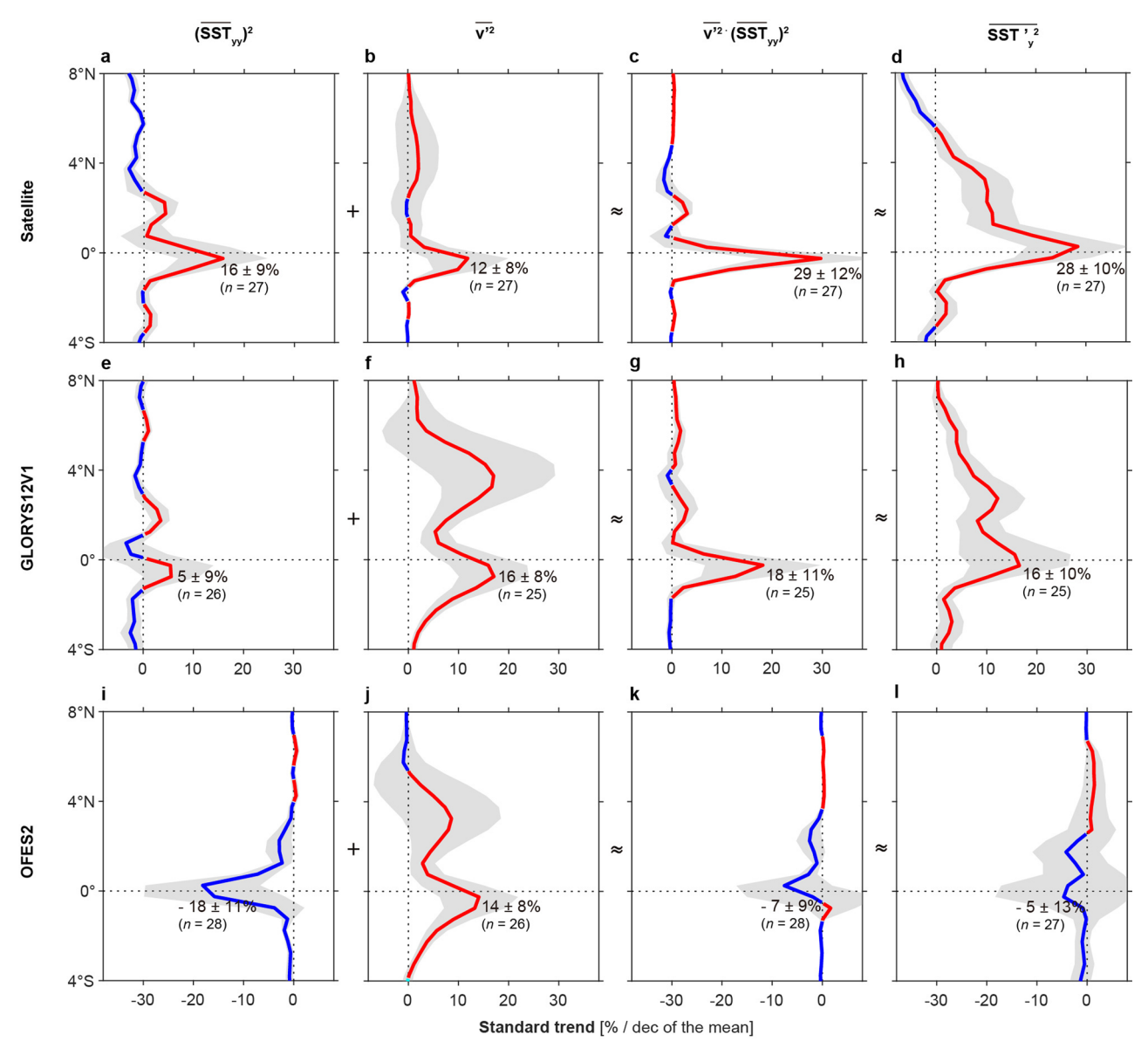
domain with westward wavelength \leq 3000 km and period \leq 40 days. Black dashed curves denote dispersion relations of free equatorial waves of the first baroclinic mode, with the phase velocity of long gravity wave at 2.8 m s⁻¹: 'RO', 'R1-3' and 'K' denote the mixed Rossby-gravity, first-third meridional-mode Rossby, and Kelvin waves, respectively. The trends are based on the 9-year running average of the spectra that are calculated over 160° W- 100° W at each year, then averaged between (1° S- 1° N) / (2° S- 2° N) for (\mathbf{a} , \mathbf{c}) / (\mathbf{b} , \mathbf{d}). Dotted regions pass the 95% confidence level based on the modified Mann–Kendall test.



Extended Data Fig. 2 | Trends based on annual mean time series.

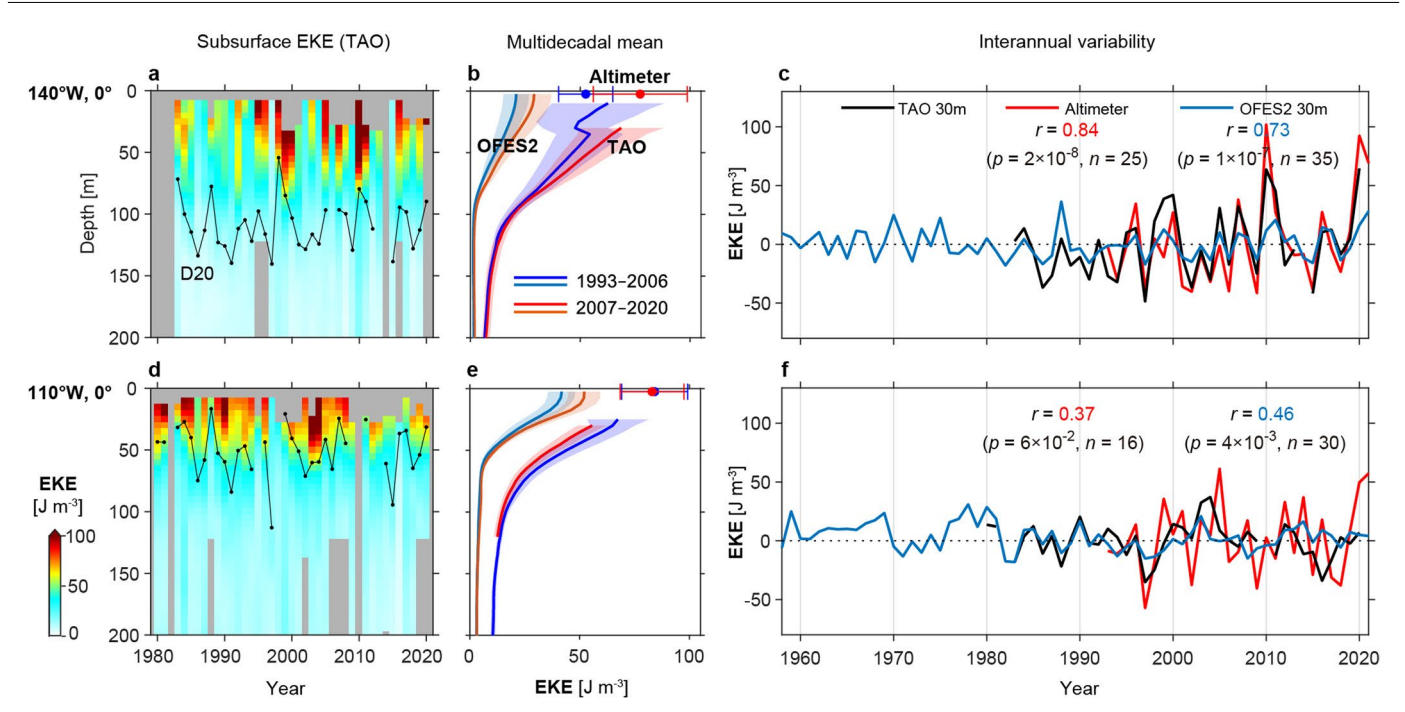
a,b, Satellite-observed $\overline{SST'_y}^2$, **c,d**, altimeter-derived EKE, and **e,f**, OFES2-simulated surface EKE. Left panels represent time series averaged in the dashed box of right panels (160°W–100°W and 1°S–1°N): annual (thin blue curves) and 9-yr running mean (bold blue curves); Dashed lines denote their fitted linear

trends (thin magenta/red for annual mean over 1993–2015/2021, and bold red for 9-yr running mean over 1993–2021). T, p, and n represent the trends (per decade) \pm uncertainties (estimated as the s.e.m.), p values, and n numbers for the statistics. Right panels represent 1993–2021 trends based the annual mean time series.



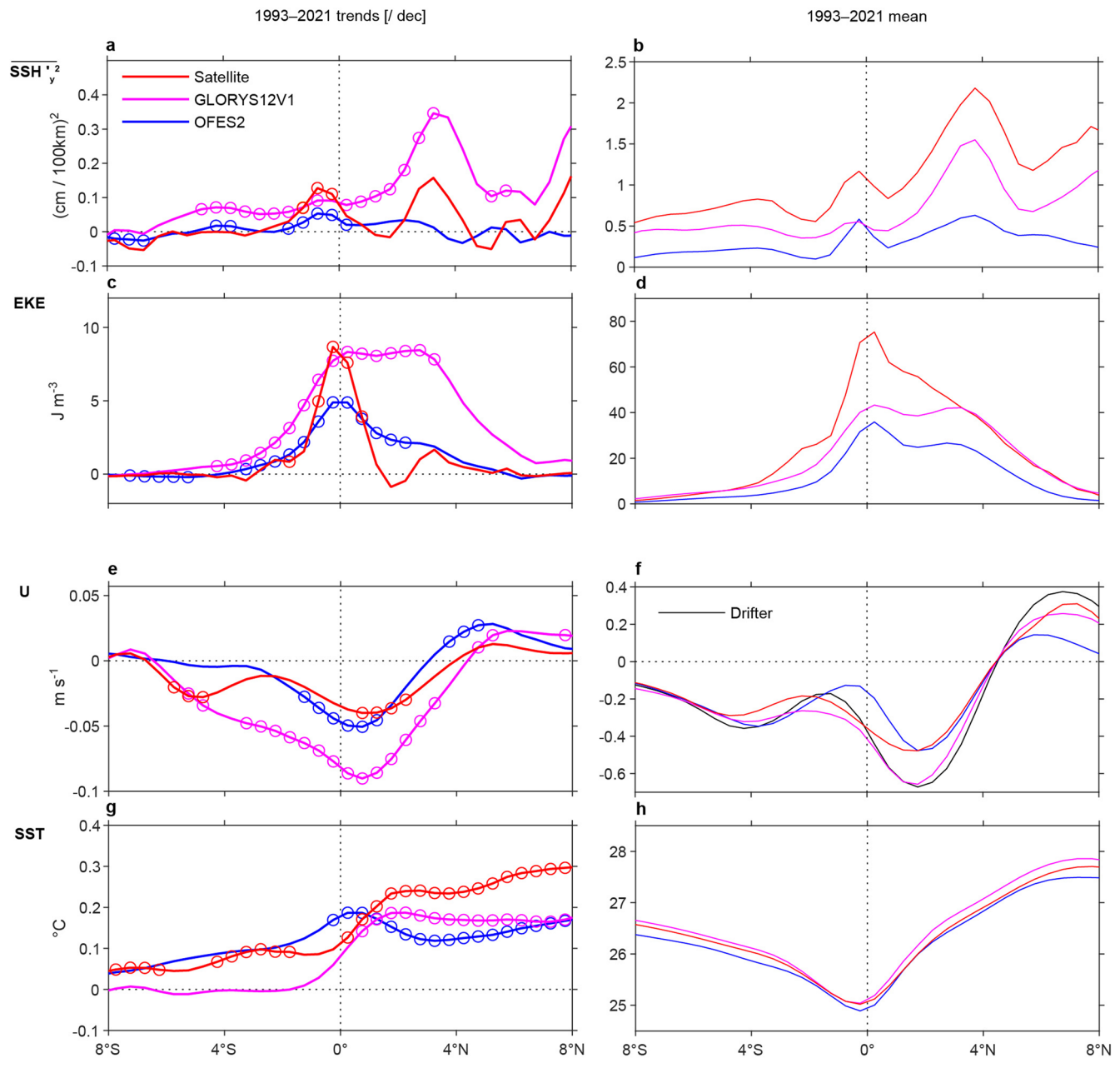
Extended Data Fig. 3 | Trends in $(\overline{SST}_{yy})^2$, $\overline{v'^2}$, $\overline{v'^2}$ ($\overline{SST}_{yy})^2$, and $\overline{SST'}_y^2$ of Eq. 3. a,e,i, $(\overline{SST}_{yy})^2$. b,f,j, $\overline{v'^2}$. c,g,k, $\overline{v'^2}$ ($\overline{SST}_{yy})^2$. d,h,l, $\overline{SST'}_y^2$. a-d, e-h and i-l are on the basis of satellite observations, GLORYS12V1 reanalysis (1993–2020), and OFES2 simulation over 1993–2021, respectively. They were averaged between

 $160^{\circ}\text{W}-100^{\circ}\text{W}$, standardized by maximum values of the climatological mean in meridional direction. Data are represented as the trends \pm uncertainties (grey shading, estimated as the s.e.m.) at the equator, with n numbers shown. The results demonstrate the proportional relationship: $\overline{\text{SST}'_{y}^{2}} \propto \overline{v'^{2}} \overline{\text{SST}}_{yy}^{2}$, at the equator (Eq. 3, Methods).



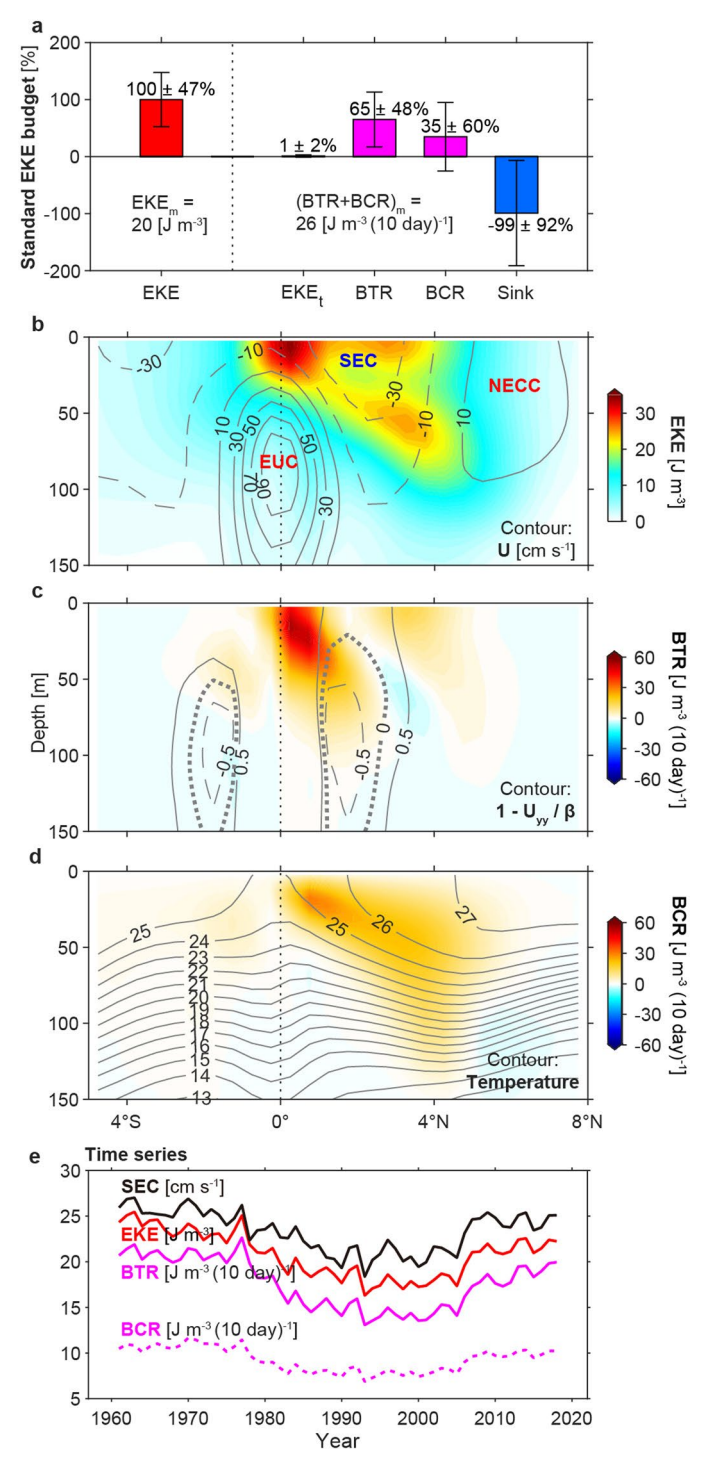
Extended Data Fig. 4 | Validation of EKE with in situ observations. Upper and lower panels denote two sites at $140^\circ W$ and $110^\circ W$ equator of the TAO array, respectively. **a,d**, Depth-temporal variation of subsurface EKE from TAO; Black curves denote thermocline defined as the depth of $20^\circ C$ isotherm (D20). **b,e**, Multidecadal mean of EKE profile from altimeter (dots on the surface), OFES2 (in CMYK color), and TAO (in RGB color) between 1993–2006 (blue curves)

and 2007–2020 (red curves); Color shading denotes the standard deviation of the time series. \mathbf{c} , \mathbf{f} , Interannual variability of EKE from altimeter (red), OFES2 at 30 m depth (blue), and TAO at 30 m depth (black), 1993–2020 mean removed. The r, p, and n denote the correlation coefficients, p values, and n numbers of the altimeter and OFES2 EKE time series with TAO based on the Student's t test.



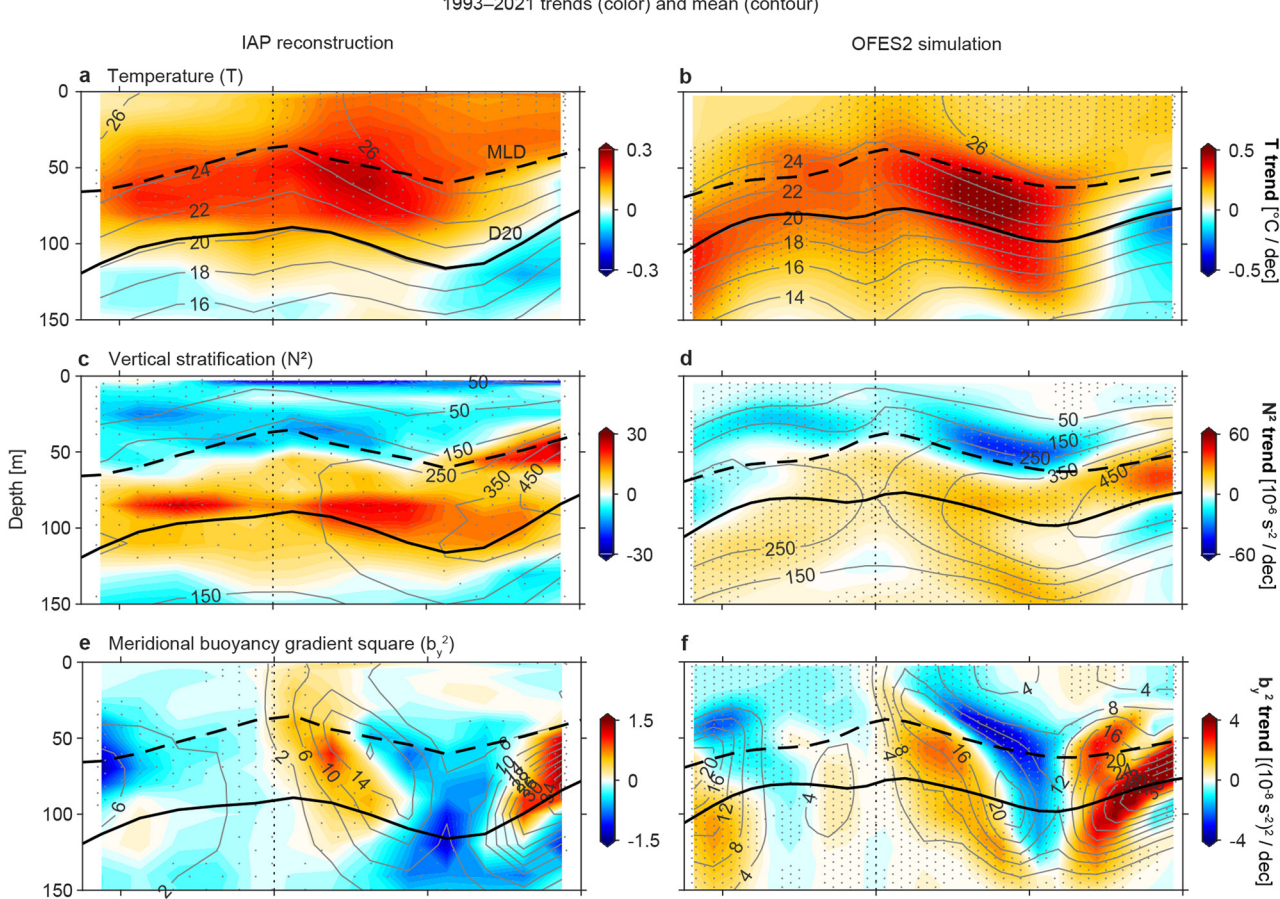
Extended Data Fig. 5 | Meridional structures of SSH_y^2 , EKE, surface zonal current, and SST trends. Left/right panels are trends/mean over 1993–2021, averaged between 160°W–100°W. a,b, \overline{SSH}_y^2 . c,d, EKE. e,f, surface zonal current. g,h, SST. They are on the basis of satellite observation or derivation (red),

GLORYS12V1 reanalysis (magenta), and OFES2 simulation (blue). Black curve in f denotes surface zonal currents from historical drifter trajectories 66 . Trends marked with circles pass the 95% confidence level based on the modified Mann–Kendall test.



Extended Data Fig. 6 | Mean states of EKE budget based on OFES2. Similar to Fig. 3, but for the climatological mean. **a**, Mean EKE and the budget terms (shaded bars); Error bars denote uncertainties as the standard deviations between 1993–2021 mostly due to interannual variability; Data are represented as the mean \pm uncertainties, with n numbers of 24, 28, 26, 24, and 25 from left to right. **b-d**, Meridional transects of mean EKE (colour shading) with zonal current

(contours, cm s⁻¹) (**b**), BTR (colour shading) with $(1-U_{yy}/\beta)$ (contours, dimensionless) (**c**) and BCR (colour shading) with temperature (contour, °C) (**d**), 160° W- 100° W averaged. **e**, 9-yr running mean time series of EKE (red), BTR (solid magenta), BCR (dashed magenta) averaged between 160° W- 100° W, 2° S- 2° N, and 0-50 m depth, and SEC speed (black) averaged between 0° - 4° N.



4°S

1993-2021 trends (color) and mean (contour)

 $Extended\,Data\,Fig.\,7\,|\,Trends\,of\,upper\,ocean\,stratifications\,in\,the\,equatorial$ Pacific. 1993–2021 trends (color shading) are superimposed with the mean states (contour, same unit as the trends without '/ dec'): a,b, Temperature; c,d, Vertical stratification (buoyancy frequency square, $N^2=-b_z$, where the buoyancy $b=-\frac{\rho}{\rho_0}g$); **e,f**, Meridional buoyancy gradient square (b_y^2) . b_y^2 is calculated

4°N

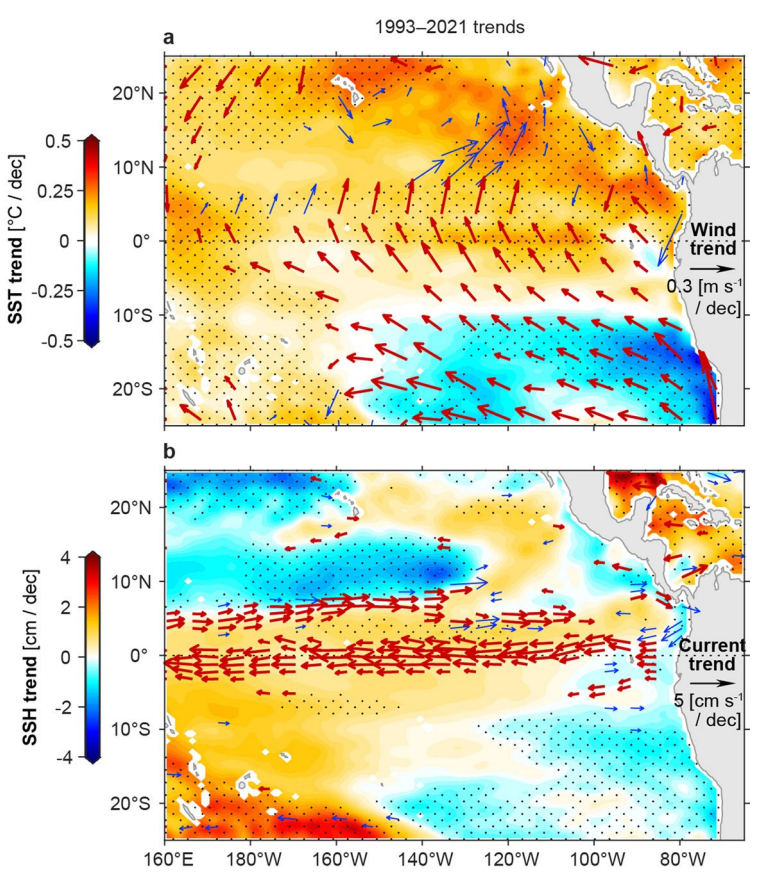
4°S

using monthly data before the average. Left/right panels are from IAP reconstruction/OFES2, averaged between 160°W-100°W. Dashed and solid black curves are climatological mean mixed layer depth (MLD) and D20, respectively. Note that the left and right have different ranges of colorbar and contour $intervals\,in\,order\,to\,magnify\,the\,structure\,of\,the\,trends.$

4°N

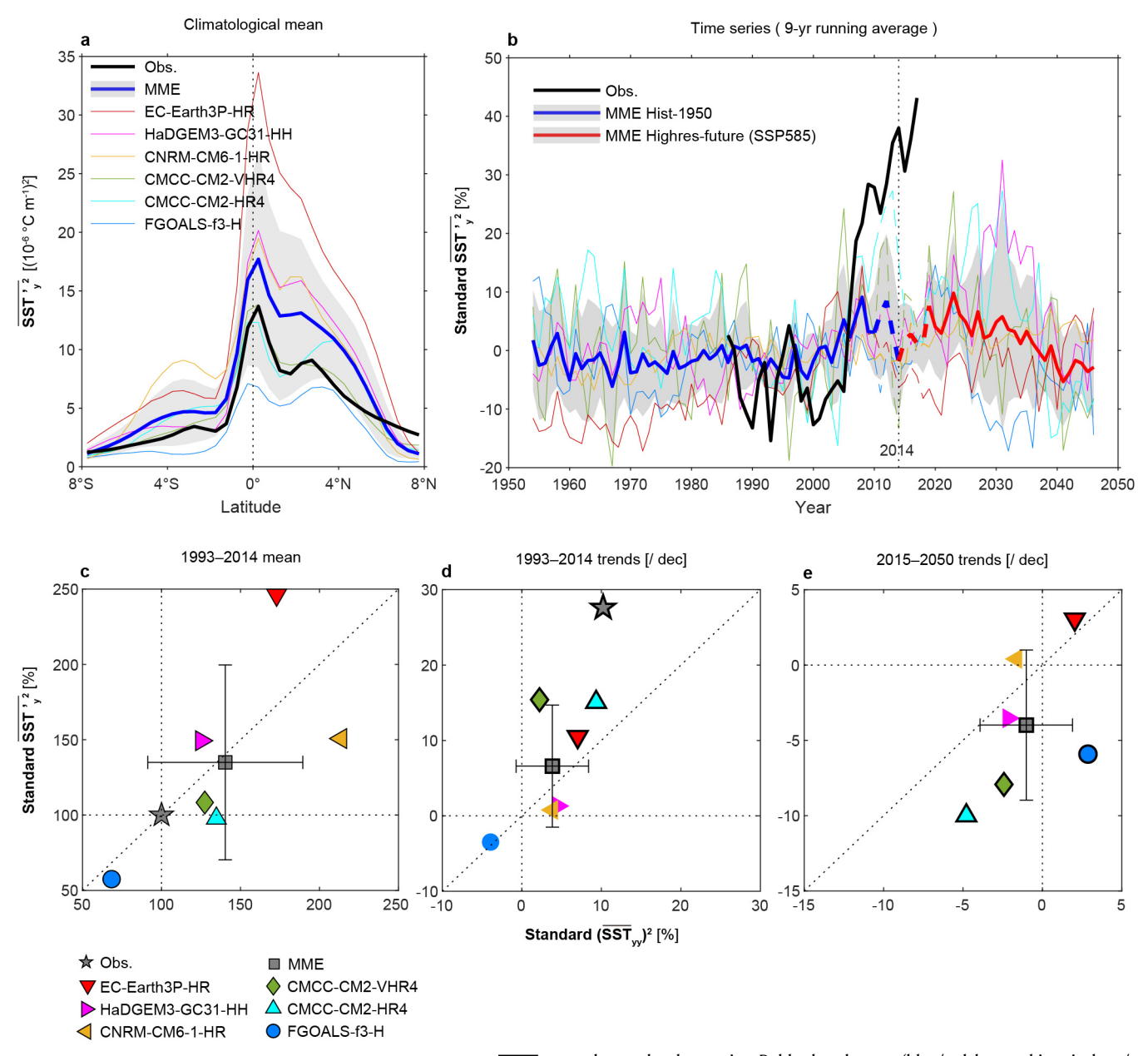
8°N

0°



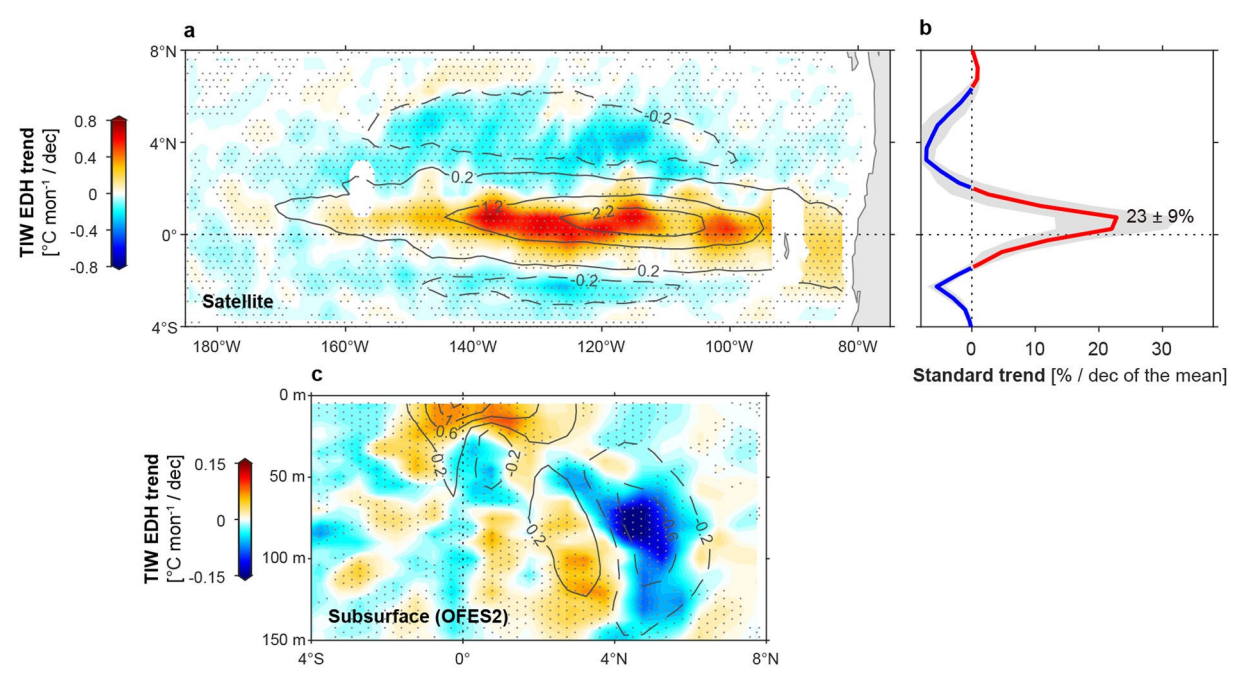
 $\label{lem:extended} \textbf{Extended Data Fig. 8} \ | \ \textbf{Trends of the tropical Pacific climate and ocean surface currents in OFES2 simulation.} \ Same as Fig. 5a,c but for the OFES2 simulation. \\ \textbf{a}, 1993-2021 \ trends of simulated SST (colour shading) \ and 10-m \ wind from JRA55-do reanalysis (vector, accelerating in bold red; decelerating in thin blue).$

 $\begin{tabular}{ll} {\bf b}, 1993-2021 trends of simulated SSH (colour shading) and surface currents (vector, accelerating in bold red; decelerating in thin blue). The JRA55-do reanalysis is the atmospheric forcing of the OFES2 simulation. \end{tabular}$



Extended Data Fig. 9 | **CMIP6 HighResMIP1-simulated and projected SST** $_{y}^{'2}$ **trends. a**, Climatological mean as a function of latitude; **b**, Long-term evolution (9-yr running mean, standardized by the 1993–2014 mean). Scatter diagrams of the standardized $\overline{\text{SST}}_{y}^{'2}$ (y axis) vs. $\overline{\text{SST}}_{yy}^{'2}$ (x axis): **c**, the 1993–2014 mean (standardized by the observation), **d**, the 1993–2014 and **e**, 2015–2050 trends (markers with black edge pass the 95% confidence level), averaged between $160^{\circ}\text{W}-100^{\circ}\text{W}$ and $1^{\circ}\text{S}-1^{\circ}\text{N}$. Black curves in **a**,**b** and grey pentagrams in **c**,**d**

denote the observation. Bold colored curves (blue/red denotes historical run/future projection) in ${\bf a}$, ${\bf b}$, and grey squares in ${\bf c}$, ${\bf d}$, ${\bf e}$ denote multi-model ensemble mean (MME) with spreads (1 s.d. of ensemble with n number of 6). The used CMIP6 HighResMIP1 ensemble consists of six coupled atmosphere-ocean models (thin curves or colored markers) with historical radiative forcing (Hist-1950 experiment: 1950–2014) and future SSP585 forcing (Highres-future experiment: 2015–2050).



Extended Data Fig. 10 | **Trends of TIW-induced EDH.** 1993–2021 trends (color shading) are superimposed with the mean states (contour, same unit as the trends without '/ dec'): **a**, Satellite-derived surface EDH; **b**, 160° W- 100° W average of **a** along with the uncertainties in percentage form, standardized by maximum values (\sim 2 °C month⁻¹) of the climatological mean in the meridional direction; Data are represented as the trends \pm uncertainties (estimated as the s.e.m.) at the

equator, with n numbers of 25. c, Meridional transect of OFES2-simulated subsurface EDH averaged between $160^\circ\text{W}-100^\circ\text{W}$. The OFES2 simulation underestimates the EDH trends because the $\overline{\text{SST}'}_{\hat{y}}^2$ trend is biased to be negative (Extended Data Fig. 3I). The OFES2 results suggest that the heating effects are amplified near the surface.